Published in final edited form as:

*Geochim Cosmochim Acta*. 2021 April 15; 299: 199–218. doi:10.1016/j.gca.2021.02.012.

# Oxygen isotope systematics of chondrules in the Paris CM2 chondrite: indication for a single large formation region across snow line

**Noël Chaumard**[a,b], **Céline Defouilloy**[a,c], **Andreas T. Hertwig**[a,d], **Noriko T. Kita**[a,*]

[a]WiscSIMS, Department of Geoscience, University of Wisconsin-Madison, 1215 W. Dayton Street, Madison, WI 53706-1692, USA.

[b]Fi Group, Direction scientifique, 14 terrasse Bellini, 92800 Puteaux, France.

[c]CAMECA, 29 quai des Grésillons, 92622 Gennevilliers Cedex, France.

[d]Institut für Geowissenschaften, Universitat Heidelberg, Im Neuenheimer Feld 234-236, 69120 Heidelberg, Germany.

## Abstract

In-situ oxygen three-isotope analyses of chondrules and isolated olivine grains in the Paris (CM) chondrite were conducted by secondary ion mass spectrometry (SIMS). Multiple analyses of olivine and/or pyroxene in each chondrule show indistinguishable $\Delta^{17}O$ values, except for minor occurrences of relict olivine grains (and one low-Ca pyroxene). A mean $\Delta^{17}O$ value of these homogeneous multiple analyses was obtained for each chondrule, which represent oxygen isotope ratios of the chondrule melt. The $\Delta^{17}O$ values of individual chondrules range from −7‰ to −2‰ and generally increase with decreasing Mg# of olivine and pyroxene in individual chondrules. Most type I (FeO-poor) chondrules have high Mg# (~99) and variable $\Delta^{17}O$ values from −7.0‰ to −3.3‰. Other type I chondrules (Mg# ≤97), type II (FeO-rich) chondrules, and two isolated FeO-rich olivine grains have host $\Delta^{17}O$ values from −3‰ to −2‰. Eight chondrules contain relict grains that are either $^{16}O$-rich or $^{16}O$-poor relative to their host chondrule and show a wide range of $\Delta^{17}O$ values from −13‰ to 0‰.

The results from chondrules in the Paris meteorite are similar to those in Murchison (CM). Collectively, the $\Delta^{17}O$ values of chondrules in CM chondrites continuously increase from −7‰ to −2‰ with decreasing Mg# from 99 to 37. The majority of type I chondrules (Mg# >98) show $\Delta^{17}O$ values from −6‰ to −4‰, while the majority of and type II chondrules (Mg# 60-70) show $\Delta^{17}O$ values of −2.5‰. The covariation of $\Delta^{17}O$ versus Mg# observed among chondrules in CM chondrites may suggest that most chondrules in carbonaceous chondrites formed in a single large region across the snow line where the contribution of $^{16}O$-poor ice to chondrule precursors and dust enrichment factors varied significantly.

### Keywords

Carbonaceous chondrites; chondrules; oxygen three-isotope measurements; SIMS analyses

[*]Corresponding author. noriko@geology.wisc.edu.

# 1. INTRODUCTION

Among carbonaceous chondrites (CCs), CM (Mighei-like) chondrites are the most abundant group (Weisberg et al., 2006). They are recognized as xenoliths in numerous other groups of CCs and meteorite classes and thus may correspond to the most abundant and/or widely dispersed material in the main belt (e.g., Zolensky et al., 1996; Gounelle et al., 2003; Bischoff et al., 2006; and references therein; Briani et al., 2012), hence their importance to deciphering the formation and evolution of the early Solar System. In addition to low to mild thermal metamorphism (e.g., Nakamura, 2006; Kimura et al., 2011; Tonui et al., 2014), CM chondrites experienced intense parent body aqueous alteration (e.g., Sears and Dodd, 1988; Brearley, 2003; Busemann et al., 2007; Schrader and Davidson, 2017). Most CM chondrites are of petrologic type 2 (e.g., McSween 1979; Kallemeyn and Wasson, 1981; Zolensky et al., 1993) and display various degrees of aqueous alteration and have been divided into petrologic subtypes from 3.0 to 2.0, where numbers decreases with increasing alteration (e.g., Zolensky et al., 1997; Rubin et al., 2007; Rubin, 2015; Kimura et al., 2020). Some CM chondrites are almost completely altered and assigned to be subtype 2.0, which was previously classified as CM1 (Zolensky et al., 1997; Rubin e al., 2007).

Paris is one of the least altered CM chondrites and has been used to investigate the early stages of the parent body aqueous alteration of CM chondrites (Hewins et al., 2014; Marrocchi et al., 2014; Rubin, 2015; Leroux et al., 2015; Pignatelli et al., 2016; Vacher et al., 2016, 2017; Verdier-Paoletti et al., 2017). Based on a detailed petrographic and mineralogical survey, Marrocchi et al. (2014) classified Paris as a CM2.7. However, Paris contains both highly and less altered lithologies (Hewins et al., 2014). Based on the PCP (Poorly Characterized Phases) index defined by Rubin et al. (2007), the less altered lithology of Paris is of petrologic subtype 2.9 (Hewins et al., 2014), which is consistent with the observation of a significant amount of Fe-Ni metal blebs and the presence of a pristine matrix (Leroux et al., 2015; Rubin, 2015). The oxygen isotope ratios of the less altered lithologies are as low as $\delta^{17}O = -2.1$‰o and $\delta^{18}O = 2.4$‰, which is at the lower end of a linear trend defined by Paris subsamples and bulk CM2 chondrites (Hewins et al., 2014). The variation of oxygen isotope ratios among bulk CM chondrites is ascribed to heterogeneity in the extent of secondary aqueous alteration processes (Clayton and Mayeda, 1999; Hewins et al., 2014). The less altered lithology of Paris thus offers a unique opportunity to investigate the origin and petrogenesis of CM chondrules.

In situ SIMS (secondary ion mass spectrometry) oxygen 3-isotope analysis of individual chondrules is a powerful tool to constrain the conditions of their formation (e.g., Kita et al., 2010; Ushikubo et al., 2012; Schrader et al., 2013; Marrocchi et al. 2018; 2019). Many chondrules in CCs contain olivine grains with heterogeneous oxygen isotope ratios (e.g., Kunihiro et al., 2004, 2005; Jones et al., 2004; Wasson et al., 2004; Connolly and Huss, 2010; Rudraswami et al., 2011; Ushikubo et al., 2012; Schrader et al., 2013; 2017; Tenner et al., 2013; Marrocchi et al., 2018; 2019). They are considered as “relict” and interpreted as unmelted material that survived the final high-temperature event of chondrule formation. Because of the slow diffusivity of oxygen isotopes in olivine (e.g., Chakraborty, 2010), these relict grains preserved their initial oxygen isotope ratios and would provide important knowledge about precursor solids that formed chondrules. However, multiple high precision SIMS analyses of olivine and/or pyroxene in each chondrules are mostly indistinguishable (e.g., Rudraswami et al., 2011; Ushikubo et al., 2012; Tenner et al., 2013; 2015; 2017; Hertwig et al., 2018; 2019a; Chaumard et al., 2018). Ushikubo et al. (2012) showed plagioclase and glass in chondrule mesostasis from Acfer 094 are in agreement with those of olivine and pyroxene phenocrysts of the same chondrules. Internally homogeneous oxygen isotope ratios within individual chondrules represent those of the final chondrule melt from which the “non-relict” olivine and other minerals crystallized.

The degree of mass independent isotope fractionation of oxygen 3-isotopes, commonly expressed as $\Delta^{17}O$ (= $\delta^{17}O - 0.52 \times \delta^{18}O$), determined for individual chondrules in CCs, systematically vary against the Mg# (= MgO/[MgO+FeO] in mol.%) of olivine and pyroxene (Ushikubo et al., 2012; Tenner et al., 2013; 2015; 2017; Hertwig et al., 2018; 2019a). Variation of Mg#s among chondrules indicates that the redox state of the environments they formed in were variable. Such variations were probably due to metal-silicate equilibria (Zanda et al., 1994) which were influenced by varying proportions of anhydrous dust, $H_2O$ ice, and organic matters relative to the solar-composition nebula gas in the outer disk regions where CC chondrules formed (e.g., Wood and Hashimoto, 1993; Grossman et al., 2008). Heterogeneous oxygen isotope ratios among chondrule precursor phases, such as $^{16}O$-rich anhydrous dust and $^{16}O$-poor $H_2O$-ice (Krot et al., 2006; Sakamoto et al., 2007), could explain the negative correlation between $\Delta^{17}O$ values and Mg# among chondrules in CCs (e.g., Connolly and Huss, 2010; Schrader et al., 2013; Tenner et al., 2015; Hertwig et al., 2018).

In contrast, $\Delta^{17}O$ values among chondrules in non-carbonaceous chondrites, such as ordinary and enstatite chondrites that likely derived from inner disk material (Kruijer et al., 2017), show narrower ranges and are $^{16}O$-depleted relative to those in CCs (e.g., Kita et al., 2010; Weisberg et al., 2011; Libourel and Chaussidon, 2011; Schneider et al., 2020). Kita et al. (2010) argued that solid precursors of ordinary chondrite chondrules were fractionated in $\delta^{18}O$ as a result of condensation of solids from $^{16}O$-poor nebula gas at high temperatures. It is likely that the oxygen isotope ratios of precursor phases were homogenized in the inner disk region prior to the formation of chondrules.

Chaumard et al. (2018) studied 29 chondrules in the Murchison CM2 chondrite and found that the distribution of Mg#s and $\Delta^{17}O$ of individual chondrules are similar to those in Acfer 094 and CO3 chondrites. Co-existing olivine and pyroxene in individual Murchison chondrules show indistinguishable oxygen isotope ratios excluding the minor occurrence of relict grains, which further indicate that chondrules solidified from numerous melt droplets with homogeneous oxygen isotope ratios. Chondrule oxygen isotope systematics in Murchison further indicated that the CO and CM chondrite parent bodies collected similar populations of chondrules, while other studies suggest that the timing of the CM parent body accretion may have been delayed relative to the CO parent body accretion (e.g., Sugiura and Fujiya, 2014).

In Murchison, chondrules have an extremely limited range of Mg#s ranging from 99.6 to 99.0 for type I chondrules (with one exception with Mg#~96) and a slightly larger range, from ~65 to ~70, for type II chondrules. The $\Delta^{17}O$ values among Murchison chondrules show a hint of systematic increase with decreasing Mg#s. Here we report *in situ* high precision SIMS oxygen 3-isotope measurements of olivine and pyroxene in chondrules from the less altered lithology of the Paris CM2 chondrite. The Paris meteorite provides an opportunity to study a diverse range of less altered chondrules in CM chondrites in petrologic context, including chondrule textures, mineralogy, and mineral chemistry (Hewins et al., 2014; Rubin, 2015; Stephant et al., 2017). This will enable us to further constrain the nature of pristine chondrules from carbonaceous chondrites in general.

# 2. ANALYTICAL PROCEDURES

## 2.1. Sample and chondrule selection

Within the less altered lithology of the Paris CM chondrite (type 2.9; Hewins et al., 2014), we selected and analyzed 29 chondrules from one polished section allocated by the Muséum national d'Histoire naturelle of Paris (MNHN 4029-11). We intended to obtain the most diverse selection of chondrules based on their size, texture, and mineralogy. Selected chondrules include 25 type I (Mg#≥90) chondrules (from ~200 μm to ~2 mm in diameter), three type II (Mg#<90) chondrules (~250–600 μm in diameter), and one fragment of a type I chondrule (~600 μm long). We also analyzed two isolated grains of FeO-rich olivine (~250–400 μm in size), one amoeboid olivine aggregate (AOA) (~500 μm long), and one FeO-poor olivine-bearing object (~400 μm long).

Nine type I chondrules are porphyritic olivine-pyroxene (POP; 20–80% modal olivine), three are porphyritic olivine (PO; >80% modal olivine), and eight are porphyritic pyroxene (PP; <20% modal olivine). One type I chondrule is barred olivine (BO) and two are composed of a BO core surrounded by a POP rim. We also analyzed one type I granular olivine (GO) chondrule and one granular olivine-pyroxene (GOP) chondrule. The fragment of the type I chondrule displays a BO texture. The three type II chondrules have a PO texture.

In all groups of CCs, chondrules are predominantly type I (e.g., Jones, 2012). It has been reported that ~95% of chondrules in CM chondrites are porphyritic, 10–40% of these porphyritic chondrules being type II (Jones, 2012; and references therein). Approximately 80% of the chondrules analyzed are porphyritic and ~13% of them are type II. This selected population is thus roughly representative of chondrules in CM chondrites. Moreover, PO, POP, and PP chondrules in our selection represent approximately 10%, 31%, and 28%, respectively, of the entire population of chondrules analyzed in this study.

## 2.2. Scanning electron microscopy and electron microprobe analysis

Backscattered electron (BSE), secondary electron (SE) imaging and energy dispersive X-ray spectrometry (EDS) analyses of chondrules were performed using a Hitachi S-3400N scanning electron microscope (SEM) at the University of Wisconsin-Madison. The accelerating voltage was set to 15 kV. The locations of SIMS analyses were selected for olivine and pyroxene grains in each chondrule that are free of cracks and other phases as identified in BSE and SE images.

We used a Cameca SXFive FE electron microprobe at the University of Wisconsin-Madison to obtain quantitative chemical analyses of olivine and pyroxene grains with an accelerating voltage of 15 keV and a beam current of 20 nA. Counting times for the peak and background were 10 and 5 s, respectively. Several standards were analyzed for matrix correction of individual elements: natural olivine and synthetic forsterite and enstatite (Mg, Si), jadeite (Na, Al), microcline (K), chromian augite (Ca), $TiO_2$ (Ti), synthetic $Cr_2O_3$ (Cr), fayalite (Fe), and synthetic $Mn_2SiO_4$ (Mn). We analyzed Mg, Al, Si, and Na with a LTAP crystal, Ca and K with a LPET crystal, Cr and Ti with a PET crystal, and Mn and Fe with a LLIF crystal. We used the Probe for EPMA™ (PFE) software (Donovan, 2015) for data reduction and matrix corrections (ZAF and fr(z)). For each analysis, we calculated the Mg# based on EPMA measurements.

### 2.3. SIMS oxygen three-isotope analysis

We performed *in situ* oxygen three-isotope analyses of olivine and pyroxene using the Cameca IMS 1280 at the WiscSIMS laboratory, University of Wisconsin-Madison. Analytical conditions and data reduction methods were generally similar to those of Kita et al. (2010) and Tenner et al. (2013, 2015) using multi-collector Faraday cups; $^{16}O$ and $^{18}O$ on multi-collector array and $^{17}O$ on a fixed mono-collector (axial detector FC2). The analyses were performed in two sessions with different primary $Cs^+$ beam conditions; a 15 μm (session #1) and 10 μm (session #2) diameters with intensities of ~3 nA and ~1 nA, respectively. During the analysis session #1 (15 μm diameter spot), secondary ion intensities of $^{16}O$, $^{17}O$, and $^{18}O$ were ~$3.5\times10^9$, ~$1.5\times10^6$, and ~$7.5\times10^6$ counts per second (cps), respectively. FC amplifier resistors were $10^{11}$ Ω for $^{17}O$ and $^{18}O$, and $10^{10}$ Ω for $^{16}O$ as in the previous studies (e.g., Kita et al., 2010), though a newer version of the FC amplifier board was used for the detection of $^{17}O$ on the axial FC2 detector. This newer FC amplifier board from Cameca (for IMS 1280-HR) shows improved thermal noise that is close to the theoretical limit (1SD ~1,300 cps for 4 s integrations) compared to the original FC amplifier board installed to IMS 1280 (1SD ~2,000 cps for 4 s integrations). Taking advantage of lower noise level on $^{17}O$, the acquisition time for a single analysis was reduced from 200 s to 100 s and the total analysis time (including pre-sputtering and secondary beam centering time) was reduced from 7 min to 4 min compared to previous oxygen 3-isotope analyses at the WiscSIMS laboratory. Analyses session #2 (10 μm) was performed at the same time that some of chondrules from the Murchison were analyzed (Chaumard et al., 2018). Secondary ion intensities of $^{16}O$, $^{17}O$, and $^{18}O$ decreased to ~$1.5\times10^9$, ~$5.5\times10^5$, and ~$2.9\times10^6$ cps, respectively. In order to reduce the noise level of the FC amplifier for $^{17}O$ analyses below $10^6$ cps intensity, we replaced the resistor and capacitor pair on the original IMS 1280 FC amplifier board by a $10^{12}$ Ω resistor and 1 pF capacitor from a Finnigan MAT 251 stable mass spectrometer (noise level was reduced to 1SD ~1,200 cps for 4 s integrations; Chaumard et al., 2018). The mass resolving power (MRP at 10% peak height) for both sessions was set to ~2200 for $^{16}O$ and $^{18}O$, and 5000 for $^{17}O$. We measured $^{16}OH^-$ at the end of each analysis to determine its contribution to the $^{17}O^-$ signal following the methods described by Heck et al. (2010). The correction of the $^{17}O^-$ signal from $^{16}OH^-$ was negligible (<0.08‰) for both standards and unknowns.

We normalized the measured $^{18}O/^{16}O$ and $^{17}O/^{16}O$ ratios to the VSMOW scale ($\delta^{18}O$ and $\delta^{17}O$ expressed as a deviation from standard mean ocean water in the unit of 1/1000; VSMOW-scale, Baertschi 1976). The external reproducibility has been determined by intermittent measurements of a San Carlos olivine (SC-Ol) standard ($\delta^{18}O$ = 5.32‰; Kita et al., 2010). We bracketed 4 to 19 unknown chondrule analyses with 8 SC-Ol analyses, 4 before and 4 after (Kita et al., 2009). External reproducibility is calculated as the 2SD of the SC-Ol brackets, with average values during session #1 (15 μm) of 0.2‰, 0.3‰, and 0.3‰ for $\delta^{18}O$, $\delta^{17}O$, and $\Delta^{17}O$, respectively. For session #2 (10 μm), the 2SD average values are 0.4‰, 0.5‰, and 0.4‰ for $\delta^{18}O$, $\delta^{17}O$, and $\Delta^{17}O$, respectively. These values represent the spot-to-spot reproducibility and were thus assigned as the uncertainties of each individual spot analysis (Kita et al., 2009). Measurements of four olivine ($Fo_{0.6\text{-}100}$), three low-Ca pyroxene ($En_{70\text{-}97}$), and one diopside ($Wo_{50}$) standards with known oxygen isotope ratios (Eiler et al., 1997; Kita et al., 2010) were used to estimate corrections for instrumental biases of unknown olivine and pyroxene analyses (EA1). The compositional ranges of standards cover those of unknowns measured.

We obtained multiple SIMS analyses per chondrule ($n$=4 to 12, typically 8) to examine the homogeneity of the isotope ratios. As in the previous studies, a specific analysis in a single chondrule is identified as a relict when its $\Delta^{17}O$ value deviates more than 0.5‰ and 0.7‰ (3SD limits of bracket standard analyses in each analysis session) from the chondrule mean (Ushikubo et al., 2012; Tenner et al., 2013, 2015; 2017; Hertwig et al., 2018; 2019a; Chaumard et al., 2018). To identify all chondrules containing rare relict grains, a multitude of analyses per chondrules (e.g., ~50; Marrocchi et al., 2018; 2019) is required; however, a total of ~8 analyses per chondrule is sufficient to identify the $\Delta^{17}O$ value of most phenocrysts that in turn represents the value of the chondrule melt, if the chondrule consists largely of minerals with homogeneous oxygen isotope ratios. Thus, we can calculate mean oxygen isotope ratios (referred to as “host chondrule” oxygen isotope ratios) from multiple analyses within each chondrule excluding relict grains. The uncertainties of host $\delta^{18}O$ and $\delta^{17}O$ values is the propagation of (i) the 2 standard error of the mean of multiple analyses that constitute the host chondrule value (=2SD/√number of analyses; 2SD of the bracket standard analyses or 2SD of multiple analyses within a chondrule, whichever is larger), (ii) the 2SE of associated SC-Ol bracketing analyses for instrumental bias correction, and (iii) the uncertainty due to the sample topography and/or sample positioning on the SIMS stage as well as uncertainty of instrumental bias corrections, estimated to be 0.3‰ for $\delta^{18}O$ and 0.15‰ for $\delta^{17}O$ (Kita et al., 2009). Because (iii) is mass-dependent and does not affect $\Delta^{17}O$, we only use (i) and (ii) for the propagated uncertainty of $\Delta^{17}O$. The uncertainties of $\Delta^{17}O$ in the relict grains are the spot-to-spot reproducibility (2SD) as determined by bracketing analyses of San Carlos olivine.

We inspected each SIMS spot by obtaining BSE and SE images using SEM after each SIMS session. Ten of 252 pits were rejected from our final dataset because they either overlapped cracks, imperfections, or display a contribution of $^{16}OH$ to the $^{17}O$ signal of ~0.1‰ or higher.

# 3. RESULTS

## 3.1. Texture, petrography, and mineralogy

Chondrules display a wide diversity of sizes and textures, as previously observed by Hewins et al. (2014) for the Paris CM chondrite. In the following summary, textural features and chemistry of chondrule minerals are described. BSE images of individual chondrules are shown in Figs. 1-4 and EA2, in which locations of EPMA and SIMS analyses are annotated. EPMA major element data for olivine and pyroxene are shown in EA3. Additional petrologic descriptions of individual chondrules can be found in EA4. Within 19 of the 29 chondrules analyzed, coexisting olivine and low-Ca pyroxene have similar Mg#s. For the other 10 chondrules, we were only able to obtain quantitative analyses either for olivine or low-Ca pyroxene. In type I chondrules where both olivine and pyroxene were analyzed, Mg#s of olivine and low-Ca pyroxene are indistinguishable, similar to type I chondrules in other pristine chondrites (e.g., Jones, 1994; Tachibana et al., 2003; Ushikubo et al., 2012; Tenner et al., 2013, 2015; Schrader and Davidson, 2017; Schrader et al., 2017; Chaumard et al., 2018; Hertwig et al., 2018; 2019a).

**3.1.1 Type I porphyritic chondrules—**Olivine in type I porphyritic chondrules is present as large anhedral phenocrysts and euhedral grains (up to ~300 μm) (Fig. 1, 2). In several chondrules (e.g., C4, C8, C7; Fig. 2a for C7), olivine is located in the cores while the pyroxene is more abundant at the periphery. In type I POP chondrules, low-Ca pyroxene often displays a poikilitic texture with numerous cracks and pores (e.g., C7; Fig. 2a). Low-Ca pyroxene was also observed as large euhedral grains, i.e., up to ~150 μm length in chondrule C7 (Fig. 2a). In type I PP chondrules, low-Ca pyroxene display less cracks and pores (e.g., C21; Fig. 1c). High-Ca pyroxene is also present in many type I porphyritic chondrules as small grains (from a few μm to ~70 μm length), either in association with Low-Ca pyroxene or olivine (e.g., C30; Fig. 1b). Olivine grains in type I porphyritic chondrules are chemically homogeneous, with an average Mg# of 99.0±0.8 (2SD) (97.6–99.8). They contain up to 0.44 wt% $Al_2O_3$, 0.84 wt% CaO, 0.67 wt% $Cr_2O_3$, and 0.46 wt% MnO. Low-Ca pyroxene grains have Mg#s ranging from 92.5 to 99.2 and compositions of $En_{89-98}Fs_{1-7}Wo_{0-4}$. We measured 0.17–2.13 and 0.30–1.07 wt% $Al_2O_3$ and $Cr_2O_3$, respectively.

The two POP chondrules C5 (Fig. 2b) and C14 (Fig. 3) contain fragments of BO chondrules in their cores with sizes of ~200 μm and ~600 μm, respectively. Olivine and pyroxene compositions do not show significant differences between BO core and POP rim (see analysis locations on BSE images in EA2 and EPMA data in EA3). There are two type I granular chondrules (C1, GOP; C9, GO) that are composed of evenly sized grains. Olivine grains in the chondrule C9 display linear trails of micron-sized inclusions of metal (Fig. 2e). Mg# of olivine and low-Ca pyroxene in these type I chondrules are all close to ~99.

**3.1.2 Type II PO chondrules—**The three type II chondrules analyzed display a porphyritic texture and are mainly composed of olivine phenocrysts. Most of the olivine grains in chondrule C15 have euhedral shapes (Fig. 4a). The chondrules C15 and C17 contain olivine grains with forsteritic cores (~20–80 μm, $Fo_{99-91}$). The ranges of olivine

Mg#s excluding forsteritic core in chondrule C15 and C17 are 58.9–77.3 and 69.9–79.7, respectively. In chondrule C22, olivine displays Mg#s ranging from 60.3–79.0. Olivine grains in these three type II chondrules contain 0.20–0.60 wt% $Cr_2O_3$ and 0.02–0.40 wt% MnO.

**3.1.3 Isolated olivine grains—**The isolated FeO-rich olivine grains G32 and G33 (Fig. 4b-c) are 200-300 µm in sizes. The Fo contents of olivine grains show ranges of 67-75 and 30-49 for G32 and G33, respectively, which becomes more FeO-rich towards the margin of grains. Another isolated object G24 is FeO-poor olivine-bearing object (Fig. 4d) with Mg# of ~99.4±0.1. The interior of the object G24 is composed of olivine that contains numerous µm-sized Fe-metal inclusions. The texture of olivine is similar to that of dusty olivine grains, in which FeO was reduced to form Fe-rich metal (Nagahara, 1981; Rambaldi, 1981).

**3.1.4 Amoeboid olivine aggregate (AOA)—**The AOA I3 texturally resembles the amoeboid olivine inclusions (AOI) previously observed by Rubin (2015) in Paris, as well as AOAs in CV and CK chondrites (e.g., Grossman and Steele, 1976; Rubin, 2013). Small grains of diopside (<5 µm) are enclosed within large, porous, forsteritic olivine grains. The AOA I3 mostly contains chemically homogeneous olivine with Mg# 99.5±0.1 and 0.35±0.11 and 0.28±0.03 wt% of $Cr^2O_3$ and MnO, respectively.

## 3.2. Oxygen isotope ratios

A total of 242 oxygen 3-isotope analyses were obtained in 2 SIMS sessions from 33 objects (including 29 chondrules) in the CM2 Paris, which are listed in EA5. Typically, 8 analyses were performed in each object at the same location as the EPMA analyses (EA2 and EA3), including multiple phases (olivine, low-Ca pyroxene, and high-Ca pyroxene) where available. Only four good analyses were obtained from BO chondrule C13 because several analyses were rejected due to significant surface roughness (EA2). Only four analyses each were taken from two FeO-rich isolated olivine grains that were relatively small (200-300 µm). We performed four analyses in AOA I13, though two were rejected after inspections of the SIMS pits. Our new data plot between the CCAM (carbonaceous chondrite anhydrous mineral; Clayton et al., 1977) and the Y&R (Young and Russell, 1998) lines, close to the PCM (primitive chondrule minerals; Ushikubo et al., 2012) line. The $\delta^{17}O$ and $\delta^{17}O$ data from chondrules range from −23‰ to +4‰ and from −25‰ to +2‰, respectively, for olivine, and from −11‰ to +2‰ and from −14‰ to −1‰, respectively, for pyroxene (Fig. 5). These ranges are very similar to those observed in chondrules from Murchison (Chaumard et al., 2018).

**3.2.1. Chondrule oxygen isotope analyses—**Table 1 lists the host oxygen isotope ratio calculated for all chondrules except for two (C9, C15), as well as their texture, Mg#, the number of measurements per mineral, and the individual analyses that were not included in host chondrule calculations. In 18 chondrules, multiple analyses within a single chondrule display indistinguishable $\Delta^{17}O$ values within the 3SD external reproducibility (0.5‰ and 0.7‰, for 15 µm and 10 µm spot analyses, respectively). These chondrules are considered to be internally homogeneous in oxygen 3-isotope ratios. Eight chondrules contain olivine grains showing $\Delta^{17}O$ values that differ by more than the 3SD external reproducibility from the average values calculated using the remaining multiple (> 5) analyses. As described in section 2.3, these olivine grains with distinct oxygen isotope ratios are considered to be relict and were not used to calculate the individual host chondrule values. In the case of chondrule C1, one each of olivine and low-Ca pyroxene show $\Delta^{17}O$ values of −9.5‰ and −7.0‰, respectively, which are significantly lower than remaining five analyses (two olivine and three low-Ca pyroxene grains) with the mean $\Delta^{17}O$ = −5.0±0.6‰ (2SD) (Fig. 6). We considered the $^{16}O$-rich olivine and low-Ca pyroxene grains as relict grains. By excluding relict grain data, we calculate the host chondrule oxygen ratios from multiple (4–11) analyses for all but two chondrules. We consider the host chondrule $\Delta^{17}O$ values to represent oxygen isotope ratios of the chondrule melt during their formation (e.g., Ushikubo et al., 2012; Tenner et al., 2013; 2015).

In chondrule C18, five olivine grains display variable $\Delta^{17}O$ value of −1.3±0.6‰ (2SD), which differ significantly from three pyroxene analyses (−3.3±0.3‰; Fig. 1a). We consider pyroxene data to represent the host chondrule value and olivine grains to be relict grains, as was discussed in previous studies (chondrule Y22 in Tenner et al., 2013; chondrule A6 in Chaumard et al., 2018). Similarly, chondrule C8 contains dusty olivine grains (SIMS spot #252, EA2 and EA5) with a $\Delta^{17}O$ value of 0.1±0.4‰, which are significantly different from the host chondrule $\Delta^{17}O$ value of −5.4±0.2‰ that are calculated from five olivine and pyroxene analyses (Table 1). In chondrule C9, seven olivine grains display homogeneous isotope ratios with the mean $\Delta^{17}O$ value of −0.15±0.43‰ (2SD), which differ significantly from a single analysis of pyroxene (−7.8‰; Fig. 2e). All olivine grains in C9 contain numerous micron-sized inclusions of metal, which suggests they are dusty olivine grains and thus are likely to be relict. The pyroxene data are more likely to represent the host value. However, since there is only a single pyroxene analysis, we do not assign it to be host $\Delta^{17}O$ value.

We also did not assign a host $\Delta^{17}O$ value to the type II chondrule C15 (Fig. 4a) that show a large range of $\delta^{18}0$ and $\delta^{17}O$ values between PCM and CCAM lines from −6.6‰ to +2.5‰ and from −9.8‰ to −1.0‰, respectively, among 8 olivine analyses. Chondrule C15 contains forsteritic olivine grains in its core ($F0_{91\text{-}99}$), indicating that these grains represent relict grains (based on FeO contents, Fe/Mn ratios; Berlin et al., 2011; Frank et al., 2014; Schrader and Davidson, 2017). This is consistent with the lower $\Delta^{17}O$ values (−4.1‰ to −6.3‰) of forsteritic olivine grains compared to those of the more FeO-rich olivine grains with variable $\Delta^{17}O$ values (−3.3‰ to −2.3‰).

Host $\Delta^{17}O$ values from most of the type I chondrules vary continuously from −7.0±0.2‰ to −3.3±0.3‰ (Fig. 6). The two other type I chondrules (C11; Fig. 1d, and C12) and the two type II chondrules (C17 and C22) display a narrow range of host $\Delta^{17}O$ values ranging from −2.5±0.2‰ to −2.1±0.2‰ (Fig. 6). Most of the relict olivine have $\Delta^{17}O$ values between ~−2‰ and −8‰ (Fig. 6) overlapping those of the host values of other chondrules. Similar observation have been made in other carbonaceous chondrites such as Acfer 094, Murchison, Y-82094, CV, CO, and CR chondrites (Rudraswami et al., 2011; Ushikubo et al., 2012; Schrader et al., 2013, 2014, 2017; Tenner et al., 2013, 2015, 2017; Hertwig et al., 2018; 2019a; Chaumard et al., 2018). Only two relict grains have $\Delta^{17}O$ values lower than −8‰; the relict grains in chondrule C1 (−9.5‰) and C14 (−13.0‰) (Fig. 6). Among the 29 relict grains analyzed, 13 (only olivine) display $\Delta^{17}O$ values between −1.6‰ and 0.2‰ (Fig. 6). Most of these were found in the chondrule C9 that contains 7 relict olivine grains with $\Delta^{17}O$ values ranging from −0.4‰ to 0.2‰ (Fig. 2e), and in chondrule C18 that contains 5 relict olivine grains with $\Delta^{17}O$ values between −1.6‰ to −0.8‰ (Fig. 1a).

**3.2.2. Oxygen isotope ratios of isolated grains and AOA—**Table 2 shows the oxygen isotope ratios of three isolated grains and AOA. Four analyses of FeO-rich olivine grains G32 and G33 are homogeneous with $\Delta^{17}O$ values of −2.7±0.5‰ and −1.9±0.3‰, respectively (Fig. 4b-c). These analyses are in agreement with type II chondrules C17 and C22. In FeO-poor olivine G24, 8 analysis of olivine are widely distributed close to PCM line with $\delta^{17}O$ and $\delta^{17}O$ values from −3.2‰ to +3.3‰ and from −5.5‰ to +1.7‰, respectively. The range of $\Delta^{17}O$ values is from −4‰ to 0‰. As shown in Fig. 4d, the core of G24 is $^{16}O$-poor ($\Delta^{17}O$: −0.8‰ to 0.0‰) compared to the coarse rim (−2‰ to −4‰).

We analyzed four spots in olivine from AOA I3. While we rejected two analyses that show numerous large cavities in their SIMS spots (EA2), the mean of $\delta^{17}O$, $\delta^{17}O$, and $\Delta^{17}O$ values of the two remaining analyses of olivine in AOA I3 are −45.5±0.5‰, −47.3±0.4‰, and −23.7±0.2‰, respectively.

### 3.3. Chondrule Mg#

Following the method of Ushikubo et al. (2012) and Tenner et al. (2013, 2015, 2017), we calculated the “host chondrule Mg#” in taking a mean value of olivine and/or low-Ca pyroxene excluding relict grains of each chondrule investigated. These values are shown in Table 1. Uncertainties of host chondrule Mg# are defined so that they represent the range of Mg#s in each chondrule, by taking differences between maxima, or minima, and the mean Mg# of olivine and low-Ca pyroxene, respectively. The host chondrules Mg#s of type I chondrules show a narrow range between 98.6 and 99.6, except for the three type I PP chondrules C31, C11 and C12, with Mg# of 97.3, 93.3 and 93.6, respectively. The host chondrule Mg#s for the type II chondrules are calculated to be ~70 by excluding obvious relict forsteritic olivine.

## 4. DISCUSSION

### 4.1. A single or two separate isotope reservoir(s)?

The $\Delta^{17}O$ values of host chondrules and isolated olivine grains (n=30) are shown in Fig. 6 in the sequence of decreasing $\Delta^{17}O$ values from −1.9 ±0.3‰ to −7.0 ±0.2‰. The majority of type I chondrules show a narrow range of $\Delta^{17}O$ between −6‰ and −4‰, while all FeO-rich chondrules and isolated olivine grains have $\Delta^{17}O$ between −3‰ and −2‰. This is very similar to the results from Murchison, where the $\Delta^{17}O$ values of high Mg# (>98) chondrules range from −6‰ to −4‰ and those of lower Mg# (96-65) chondrules are between −3‰ and −2‰ (Chaumard et al., 2018). Compared to Murchison data, Paris chondrule data are more continuous, without a gap between −4‰ and −3‰ and extend to lower $\Delta^{17}O$ ~ −7‰.

In Fig. 7, the host chondrule $\Delta^{17}O$ values in Paris are shown against their Mg#s along with data from Murchison (Chaumard et al., 2018). The majority of type I chondrules in Paris plot at highest Mg#s ~99 with $\Delta^{17}O$ from −6‰ to −4‰, while the rest of data plot on a trend where $\Delta^{17}O$ values increase with decreasing Mg#s. In Murchison, chondrules with high Mg#s (>98.5) display host $\Delta^{17}O$ values ranging from −6.0‰ to −4.1‰ while chondrules with lower Mg# (~96–65) have host $\Delta^{17}O$ values of ~−2.5‰. Thus, the chondrule Mg#-$\Delta^{17}O$ relationship in Paris is nearly the same as that observed for Murchison. Indeed, the two isolated FeO-rich olivine grains analyzed in Paris plot along and extend the trend defined by type II chondrules (in both Paris and Murchison), towards lower Mg#s (~37 for the grain G33) than was previously measured in Murchison. One PP (C31) and one POP (C18) chondrule with host $\Delta^{17}O$ values of −3.3‰ also plot between Mg# ~96–99 and two other PP chondrules (C11, C12) with $\Delta^{17}O$ values of ~−2.5‰ have Mg#s ~93-94, a range of Mg#s not found in Murchison (Chaumard et al., 2018). Thus, by combining data from two CM chondrites, CM chondrule data define a single continuous trend of increasing $\Delta^{17}O$ values with decreasing Mg#s. Marrocchi et al. (2018) also reported similar host chondrule $\Delta^{17}O$ values and Mg# data for three chondrules in NWA 5958, which is a CM-related ungrouped carbonaceous chondrite.

The Mg#-$\Delta^{17}O$ relationship among chondrules observed in CM chondrites is similar to those obtained from Acfer 094 (Ushikubo et al., 2012) and the Y-81020 CO chondrite (Tenner et al., 2013), as shown in Fig. 8, and to a lesser extent for chondrules in the Y-82094 ungrouped carbonaceous chondrite and CV chondrites (Tenner et al., 2017; Hertwig et al., 2018; 2019a). However, chondrules in Acfer 094 and Y-81020 display a well-defined bimodal distribution of $\Delta^{17}O$ at ~ −5‰ and −2.5‰ (Fig. 8). Ushikubo et al. (2012) and Tenner et al. (2013) argued that these chondrules formed in two distinct isotope reservoirs; (1) a reducing environment at lower dust enrichments (100 × solar composition gas) in which chondrules with Mg#>97 and $\Delta^{17}O$ ~ −5‰ formed and (2) an oxidizing environment showing higher dust enrichments (1000× solar) in which chondrules with Mg# <97 chondrules and $\Delta^{17}O$ ~ −2.5‰ formed. They interpreted the difference in oxygen isotope ratios between the two reservoirs as a result of varying amounts of $^{16}O$-poor $H_2O$ ice mixed in with other chondrule precursor solids.

Chondrule data from Acfer 094 and Y-810202 overlap almost exactly with the CM chondrule trend (Fig. 8), so that the two separate isotope reservoirs indicated from earlier studies could represent subsets of a single chondrule-forming region, which could have been shared by many CC chondrules. Chondrules in the ungrouped carbonaceous chondrite Y-82094 also show a similar Mg#-$\Delta^{17}O$ relationship that overlaps with that of CM chondrites. In CV chondrites, chondrules generally have high Mg#s (>98) with $\Delta^{17}O$ values predominantly ranging from −6‰ to −4‰ (Hertwig et al., 2018; 2019a; Marrocchi et al., 2019). These values overlap exactly with the CM chondrule data for Mg#>98. In all these CCs, type I chondrules with Mg#≤97 and $\Delta^{17}O$ values between −4‰ and −3‰ are scarce. The Paris chondrule C31 (PP) with Mg# ~97.3 (+0.5/−1.6) shows intermediate $\Delta^{17}O$ = −3.3±0.2‰ and is located in the gap between the two groups of chondrules ($\Delta^{17}O$ ~−5‰ and ~−2.5‰ on the $\Delta^{17}O$ versus Mg# plot, Fig. 8), so is one of the three chondrules studied by Marrocchi et al. (2018) in NWA 5958 with Mg# ~95 and $\Delta^{17}O$ of −3‰. Identifying more chondrules with intermediate Mg#s and $\Delta^{17}O$ values would further test if CC chondrules derived from a single continuous region, or if they were derived from two separate reservoirs in terms of time and locations, as argued earlier from Acfer 094 and CO chondrite chondrule data (Ushikubo et al., 2012; Tenner et al., 2013).

### 4.2. Nature of the oxygen isotope reservoir(s)

Tenner et al. (2015) presented a mass balance model to describe the observed negative correlation between $\Delta^{17}O$ values and Mg#s among CR chondrules. As discussed by Tenner et al. (2015), Mg#s of olivine and pyroxene in chondrules mainly depend on the redox state of iron that in turn was controlled by the oxygen fugacity of the chondrule-forming environment. Equilibrium thermodynamic calculations (e.g., Ebel and Grossman 2000) indicate that type I chondrules with high Mg#s formed under reducing conditions, e.g., $fO_2$ ~3.5 to ~2.5 log units below the IW buffer for Mg# 99 and 96, respectively (Tenner et al., 2015). In the protoplanetary disk, $H_2O$ ice would reside in fine-grained dust particles enriched in organic matter and amorphous silicates, similar to chondritic porous interplanetary dust particles and the matrix in primitive meteorites (e.g., Bradley and Brownlee, 1986; Abreu et al., 2010). Therefore, the model supposes that the chondrule-forming region consisted of varying relative proportions of these components. In the scope of the model, $H_2O$ ice, anhydrous dust, organics, and solar-composition gas possessed $\Delta^{17}O$ values of 5.1‰, −5.9‰, 11.3‰, and −28.4‰, respectively (Tenner et al., 2015).

The model assumes that chondrules formed in an environment whose effective oxygen isotopic composition and redox state is mostly controlled by the mixture of these four components. During transient heating, this environment comprised the solar-composition gas enriched in the evaporated portions of the precursors (= ambient gas), a melt component, and unmelted solids. Being a mixing model, no predictions are made about the actual physical processes operating during chondrule formation. It is implied by the model, however, that after evaporation, recondensation into the melt (e.g., Libourel et al., 2006; Nagahara et al., 2008; Libourel and Portail, 2018) lead to an effective oxygen exchange between melt and ambient gas (e.g., Kita et al., 2010; Ushikubo et al., 2012; Tenner et al., 2015; Marrocchi and Chaussidon, 2015; Marrocchi et al., 2019), so that melt and ambient gas display the same effective $\Delta^{17}O$ value at the time of olivine crystallization. The Mg#s of olivine and pyroxene in chondrules would be determined by the oxygen fugacity of the ambient gas, which can be estimated from the relative abundances of H, C, and O of the mixture of ambient gas and the melt component. Further details of the mass balance model are described in Tenner et al. (2015; 2018).

Using the model calculation, Tenner et al. (2015) suggested that the majority of type I chondrules in CR chondrites formed at a dust enrichment factor of 100-200 relative to solar-composition gas and with a $H_2O$-ice enhancement of 0-0.8 times relative to CI-composition dust. Subsequently, Hertwig et al. (2018) modified the model parameters by applying $\Delta^{17}O$ values of the anhydrous dust and $H_2O$ ice of −8‰ and +2‰, respectively, in order to explain the distribution of Mg#s and $\Delta^{17}O$ values of chondrules in CV chondrites. These parameters were estimated based on the assumptions that (1) the lowest host-chondrule $\Delta^{17}O$ value is representative of the anhydrous silicate dust component and (2) the average $\Delta^{17}O$ value of type II chondrules constrain the $\Delta^{17}O$ values of $H_2O$ ice based on the oxygen isotope mass balance at high dust enrichments (Tenner et al., 2015). In Paris, the lowest host $\Delta^{17}O$ value measured is −7.0‰, while the type II chondrules and FeO-rich olivine G33 reach $\Delta^{17}O$ values as high as ~ −2‰. Consequently, the $\Delta^{17}O$ values for anhydrous silicate dust and $H_2O$ ice used by Hertwig et al. (2018) are useful to estimate both the dust and $H_2O$

enrichments of the precursors during the formation of CM chondrules. Applying the model of Tenner et al. (2015) and the calculations of Hertwig et al. (2018), Mg# ~99 chondrules in Paris correspond to dust enrichment factors of 50-100× relative to solar-composition gas and to amounts of $H_2O$ in the dust ranging from 0 (anhydrous dust) to 0.8× relative to the nominal abundance of $H_2O$ ice in the CI dust (Fig. 9). For chondrules with Mg#s lower than 98 and down to mostly 60-70, the ice enrichment factor is roughly constant (between 0.8 and 1× the nominal abundance of $H_2O$ ice, relative to the CI dust) while the dust enrichment factor increases from ~100× to ≥1,000× (Fig. 9). We note that Mg# should be controlled not only by oxygen fugacity, but also by iron abundance of the system relative to Mg and Si, which is assumed to be CI chondritic in the model. Chondrules with lower Mg# (<60 down to ~35) might have been formed from precursors that were significantly enriched in iron and may not represent chondrule formation under extremely high dust-enrichments (>3,000×).

The observed relationship between $\Delta^{17}O$ values and Mg#s from chondrules in CM chondrites might have resulted from their formation in a single large region in the protoplanetary disk that was radially zoned with respect to the effective $\Delta^{17}O$ values, possibly due to variable abundances of $^{16}O$-poor $H_2O$ ice. The region would likely have existed near to the snow line, the condensation front of $H_2O$ ice. Inside the snow line, the relative abundance of $^{16}O$-poor $H_2O$ ice among the solid chondrule precursors was low in contrast to outside of the snow line (e.g., Morbidelli et al., 2016). The most reduced chondrules (Mg#s >99) formed inside the snow line, within this large region, where dust enrichment factors were up to ~100×. More oxidized chondrules with higher $\Delta^{17}O$ values and lower Mg#s would have formed towards the external part of this single chondrule-forming region where there was addition of $^{16}O$-poor $H_2O$ ice to the nearly anhydrous chondrule precursors and/or an increase of the dust enrichment factor from ~ 100× to ~1,000×, as proposed for CR chondrites by Tenner et al. (2015).

Alternatively, systematic changes in Mg#-$\Delta^{17}O$ could have developed over time. Most type I chondrules with Mg#>97 and lower $\Delta^{17}O$ values ~ −5‰ formed in regions mainly inside of the snow line with dust enrichments lower than ~ 200×. The local disk temperatures would decrease with time and, consequently, the snow line could migrate through the chondrule forming regions. At the same time, the dust layer became thicker prior to the formation of asteroidal bodies (e.g., Alexander et al., 2008). Later-forming chondrules would form under oxidizing environments and with higher $\Delta^{17}O$ values ~ −2‰ due to addition of $^{16}O$-poor $H_2O$ ice to chondrule precursors.

Hartlep and Cuzzi (2020) estimated dust enrichment factors of the turbulent disk midplane to be typically −100× where cm-sized pebbles formed by streaming instability. They further discussed that chondrules and their precursors existed in the form of cm-sized pebbles and argued that the estimated particle concentrations are consistent with those of high Mg# chondrules, which are abundant in carbonaceous chondrites. Their model also predicts that particle concentrations may reach −1,000×, but probability is low. Therefore, in principle, formation of type II chondrules under higher dust-enrichment factors of −1,000× might have occurred in the protoplanetary disk.

Many type I POP chondrules show a mineralogical zoning with olivine grains being located in the core and pyroxene in periphery of individual chondrules (e.g., Krot et al., 2004; Hezel et al., 2006; Friend et al., 2016). Further, Villeneuve et al. (2020) observed a large mass-dependent Si isotope fractionation in type I chondrules, especially in those with high Mg#s. Both observations provide evidence for SiO molecules condensing from the ambient gas to the melt. Based on detailed CL-mapping of chondrule minerals and correlated oxygen isotope systematics, Marrocchi et al. (2019) proposed that SiO (along with Mg atoms) condensing from an $^{16}$O-poor nebula gas ($\Delta^{17}$O ~0‰) interacted with $^{16}$O-rich AOA-like chondrule precursors ($\Delta^{17}$O ~ −20‰) to form type I chondrules with $\Delta^{17}$O values ranging from −6‰ to −3‰. However, 2-3 Ma after CAIs, ambient temperatures of the protoplanetary disk should have been significantly lower than the condensation temperature of Si (e.g., Desch et al., 2018). Hence, the partial pressure of SiO in the nebula gas is expected to be low, prior to the heating events causing chondrule formation. Instead, heating and evaporation of solid precursors, such as silicates, during chondrule formation would produce the majority of gaseous SiO, residing in the ambient gas (e.g., Nagahara et al., 2008) and being available for exchange and interaction with the chondrule melt and solids. Thus, the observed correlation of $\Delta^{17}$O values and Mg#s is better explained by the contribution of $^{16}$O-poor $H_2O$ ice (or icy fine-grained dust) rather than addition of $^{16}$O-poor SiO gas from nebula gas.

### 4.3. Origin of relict grains in CM chondrules

Some chondrules contain grains predating the host minerals that crystallized from the final chondrule melts. These grains are defined as relict grains and can be identified chemically and/or isotopically (e.g., Jones et al., 2004; Kunihiro et al., 2004; Krot et al., 2006; Rudraswami et al., 2011; Ushikubo et al., 2012; Schrader et al., 2013; Tenner et al., 2013; Schrader and Davidson, 2017; Hertwig et al., 2018; 2019a; Chaumard et al., 2018; Marrocchi et al., 2018; 2019). Ten of the 27 chondrules in this study contain relict olivine and/or low-Ca pyroxene grains (Table 1, Fig. 6). The abundance of relict-grain bearing chondrules (~37%) in Paris is similar to Murchison (CM2) (~38%; Chaumard et al., 2018), Acfer 094 (~ 45%; Ushikubo et al., 2012), and the Y-81020 CO chondrite (~ 42%; Tenner et al., 2013). We note that the abundance of relict-grain bearing chondrules in these chondrites is probably underestimated due to the limited number of analyses per chondrules (≤8), in comparison to the 30-50 analyses per chondrules performed in other studies (Marrocchi et al., 2018; 2019). While eight out of the nine relict grains in Murchison chondrules were $^{16}$O-rich compared to their host chondrules (Chaumard et al., 2018), four out of 10 chondrules in Paris contain relict olivine grains with $\Delta^{17}$O values higher than their host chondrules, which reach as high as 0‰. This difference might be due to selection bias for chondrules in Paris in this work (or in Murchison in previous work) and may not be statistically significant. Similar $^{16}$O-poor relict olivine grains have also been reported from other CCs but seem to be not as common (Ushikubo et al., 2012; Tenner et al., 2013; Hertwig et al., 2018; 2019a; Marrocchi et al., 2018; Schrader et al., 2020).

In type II chondrules, forsteritic cores in FeO-rich olivine phenocrysts are easily recognized as relict grains (e.g., Jones, 1990; Wasson and Rubin, 2003; Ruzicka et al., 2007, 2008). These observations indicate that at least a part of the type II chondrule precursors formed in more reducing conditions, similar to those during formation of type I chondrules (e.g., Ruzicka et al., 2008). Based on re-heating experiments of type I precursor materials at 1450–1500°C under oxidizing conditions (between the IW and NNO buffers), Villeneuve et al. (2015) proposed that type I chondrules (or fragments) could have been the main precursor material of type II chondrules. These results and the recognition of $^{16}$O-rich relict grains in the type II chondrule C17 with $\Delta^{17}$O values similar to those of host type I chondrules (Fig. 6) support this precursor origin of type II chondrules. There are many other examples where type II chondrules enclose FeO-poor olivine grains that are similar to those observed in type I chondrules (Kunihiro et al. 2004; 2005; Ushikubo et al., 2012; Tenner et al. 2013; 2017; Krot and Nagashima, 2017; Krot et al., 2018). Villeneuve et al. (2020) reported negative $\delta^{30}$Si in relict olivine from type II chondrules in carbonaceous chondrites, indicating they could have originated from forsteritic olivine of type I chondrules.

Thirteen relict grains from 7 chondrules have $\Delta^{17}$O values within the range of the host values calculated for chondrules (from −7.0‰ to −2.1‰; Fig. 6). Including the $^{16}$O-rich relict olivine in type II chondrules, it had been suggested that most relict grains were result of mixing between two distinct major isotope reservoirs (e.g., Jones et al., 2005; Hewins and Zanda, 2012; Ushikubo et al., 2012; Tenner et al., 2013, 2015). The new dataset for Paris chondrules instead may point to mixing within a single chondrule-forming region. Within this region, the radial transport of solids would have occurred (Cuzzi et al., 2010) between an inner area, enriched in reduced and $^{16}$O-rich chondrules, and an outer area, enriched in more oxidized and $^{16}$O-poor chondrules.

The remaining relict grains are significantly $^{16}$O-rich ($\Delta^{17}$O: −13‰ and −9.5‰) or $^{16}$O-depleted ($\Delta^{17}$O: from −1.9‰ to 0.2‰; Fig. 6). Similar $^{16}$O-rich relict grains were also reported in Murchison chondrules, reaching values of down to −18‰ (Chaumard et al., 2018). The $^{16}$O-rich relict grains might be related to CAI and AOA-like refractory precursors (Ushikubo et al., 2012; Marrocchi et al., 2019), which formed during the earliest stage of the Solar System evolution (≤0.2 Ma; Kita et al., 2013). However, relict olivine grains in some chondrules (C1 and C14) do neither show any special textural nor major-element compositional difference compared to other coexisting (non-relict) olivine in the same chondrules. Identification of small differences in minor elements would require detailed elemental mapping of olivine at a high electron-beam intensity, as demonstrated by Marrocchi et al. (2018; 2019) who found that relict grains tend to have lower Ca, Ti, and Al concentrations. In contrast, chondrules C8 and C9 and the isolated olivine grain G24 all show dusty olivine textures and $\Delta^{17}$O values ~ 0‰, which are significantly higher than other olivine analyses in the same objects (Table 1). Schrader et al. (2020) reported $^{16}$O-poor dusty olivine with $\Delta^{17}$O ~ 0‰ in four type I chondrules from Murchison and Murray CM chondrites and suggested that precursors of dusty olivine in CM include those unrelated to type I and II chondrules, but originated instead from an unequilibrated ordinary chondrite source. Dusty olivine grains are thought to form by the reduction during partial melting of more FeO-rich olivine, derived from a previous generation of chondrules (Nagahara, 1981; Rambaldi, 1981; Jones and Danielson, 1997; Leroux et al., 2003). Consequently, their oxygen isotope ratios likely reflect those of the FeO-rich precursors. Our results from C8, C9 and G24 are consistent with those of Schrader et al. (2020) and imply an origin of these relict grains from a different reservoir than the one in which type I ($\Delta^{17}O$: ~−5‰) and type II ($\Delta^{17}O$: ~−2.5‰) chondrules in CM and other groups of CCs formed.

The $^{16}O$-poor relict grains may be related to OC-like chondrules in CCs that show homogeneous oxygen isotope ratios with $\Delta^{17}O$ ~0‰ (e.g., Tenner et al., 2017). Tenner et al. (2017) argued that three type II chondrules in Y-82094 (ungroup C) are characterized by intermediate Mg#s (80-90), higher MnO contents in olivine, and oxygen isotope ratios on the terrestrial fractionation line but to the left side of the PCM line, which are similar to chondrules in ordinary chondrites. Recently, Williams et al. (2020) and Schneider et al. (2020) obtained coordinated $\varepsilon^{54}Cr$, $\varepsilon^{50}Ti$, and SIMS oxygen isotope analyses of individual chondrules from multiple chondrite groups and found that chondrules generally show isotope signatures similar to those of their host bulk meteorites. However, Williams et al. (2020) also found three BO chondrules in Allende (CV) with Mg#s of 80-90 that show negative $\varepsilon^{54}Cr$ and $\varepsilon^{50}Ti$ values and $\Delta^{17}O$ =0‰, which are very different from those of the bulk Allende meteorite. These chondrules do not exactly match ordinary chondrite chondrules, but show similar isotope ratios to achondrites.

The Al-Mg ages of two OC-like chondrules in Acfer 094 are older by 0.4-0.8 Ma than other chondrules in the same meteorite (Ushikubo et al., 2013; Hertwig et al., 2019b). The age difference could represent the transit time for these chondrules to travel from the outside of the CC chondrule forming regions to the Acfer 094 accretion region. Schrader et al. (2020) and Williams et al. (2020) suggested that dusty olivine in CM chondrite chondrules and the FeO-rich BO chondrules in Allende, respectively, had migrated outward from inner to outer disk across the Jupiter's gap. Collectively, both refractory $^{16}O$-rich precursors and OC-like $^{16}O$-poor precursors represent inner disk solids that would have been added to the solid precursors of CM chondrules.

## 4.4. Oxygen isotope ratios of AOA in CM

Here we compare oxygen isotope ratios of AOA I3 in Paris obtained during this work to AOAs in other CCs and refractory inclusions in CM chondrites, which were previously obtained in the WiscSIMS laboratory. The mean of 2 analyses of AOA I3 gives $\delta^{17}O$ = −45.5±0.5‰, $\delta^{17}O$ = −47.3±0.4‰, and $\Delta^{17}O$ = −23.7±0.2‰ (Table 1). This is in agreement with AOA analyses in Acfer 094 (mean of four AOA and 2SD; $\delta^{17}O$ = −45.8±0.7‰, $\delta^{17}O$ = −47.7±0.7‰, and $\Delta^{17}O$ = −23.8±0.6‰; Ushikubo et al., 2017) and those in DOM 08006 (CO3.0; $\delta^{17}O$ = −45.8±0.7‰ and $\Delta^{17}O$ = −24.0±0.4‰; Fukuda et al., 2021). Data from I3 are also consistent with spinel-hibonite inclusions (SHIBs) in Murchison studied by Kööp et al. (2016) with $\Delta^{17}O$ = −23.4±1.1‰. Other studies reporting oxygen isotope ratios of AOA from multiple CCs (Fagan et al., 2004; Krot et al., 2005; 2014; Komatsu et al., 2017), Kakangari (Nagashima et al., 2015), ordinary chondrites (Itoh et al., 2007; Ebert et al., 2020), and enstatite chondrite (Guan et al., 2000) also show similar ranges. Thus, AOA I3 formed in a homogeneous $^{16}O$-rich isotope reservoir that formed a wide variety of CAIs (e.g., Ushikubo et al., 2017).

### 4.5. Implications for the chondrule formation region

The large chondrule formation region discussed in 4.2. would likely be located at around 3 AU, where the snow line would be located at the time of chondrule formation (a few Ma after CAIs; Morbidelli et al., 2016). This region would have been outside of the OC chondrite accretion region, so that a minor fraction of inner disk materials might have been transported from the inner disk to the outer disk (Hertwig et al., 2018; Schrader et al., 2020; Williams et al., 2020). Several recent studies suggest that CM and other CCs form outside of proto-Jupiter in order to explain the isotope dichotomy between carbonaceous meteorites and non-carbonaceous meteorites (e.g., Kruijer et al., 2017; Desch et al., 2018; Nanne et al., 2019; Van Kooten et al., 2020), a hypothesis first advocated based on bulk meteorite nucleosynthetic anomalies of $^{54}Cr$ and $^{50}Ti$ by Warren (2011). Kruijer et al. (2017) further suggested that the isolation of carbonaceous and non-carbonaceous isotope reservoirs occurred early, within 1 Ma after CAI formation. This predates the events forming CC chondrules which are estimated to have occurred 2-3 Ma after CAI formation (e.g., Ushikubo et al., 2013; Nagashima et al., 2017; Hertwig et al., 2019b). Desch et al. (2018) proposed a comprehensive evolutionary model involving the proto-Jupiter’s gap that predicts a location and formation time for each meteorite parent body in order to explain the chemical diversity among meteorites. In their model, Jupiter originally formed ≥4 AU and migrated inward to 3 AU to open a gap that separated the two isotope reservoirs. Within this framework, chondrules in CCs should form beyond the snow line, which is in contrast to the dry environments expected for the abundant CM chondrules with high Mg# (>98) and $\Delta^{17}O$ ~−5‰. Furthermore, complete isolation of carbonaceous and non-carbonaceous meteorite forming regions can not explain chondrules and relict grains with OC-like oxygen isotope ratios in CM chondrites. Schrader et al. (2020) argued that small fragments of UOC chondrules (<300 μm) could migrate outward beyond the Jupiter’s gap and so were incorporated to chondrule precursors for CM chondrites. A few chondrules in Paris contain dusty olivine grains with $\Delta^{17}O$ ~0‰ (C8, C9, C24), which are also ~300 μm or smaller and could have migrated from UOC regions across the Jupiter’s gap. Chondrules with $\Delta^{17}O$ ~0‰ in Acfer 094 and Y-82094 (ungrouped C) are also ≤300 μm in size, though those in CV are from ~ 500 μm (Hertwig et al., 2018; 2019) to ≥ 2 mm (Williams et al., 2020).

Alternatively, proto-Jupiter could have been located close to the current Jupiter orbit that is outside of the major CC chondrule-forming regions. Recent numerical simulation by Tanaka et al. (2020) indicated that Jupiter-sized giant planets would not experience a significant radial migration as opposed to those indicated in previous studies (e.g., Lin and Papaloizou 1986). If there were radial transport of solids in the protoplanetary disk (e.g., Cuzzi et al., 2010), a small amount of OC-like chondrules and their fragments could have migrated outward to CM and other major CC forming regions. The main drawback in this scenario is that inward drift of significant amounts of dust from the CC forming regions to the OC forming regions might have occurred. This would be in disagreement with the observed distinct isotope signatures between bulk carbonaceous and non-carbonaceous meteorites (e.g., Budde et al., 2016; Kruijer et al., 2017; Kleine et al. 2020).

## CONCLUSIONS

In situ SIMS oxygen 3-isotope analyses of 29 chondrules and 3 isolated olivine grains in the least-altered CM chondrite Paris were performed. The results were used to estimate host chondrule $\Delta^{17}O$ values. By combining this data set with that from Murchison chondrules (Chaumard et al., 2018), the Mg#- $\Delta^{17}O$ relationship of CM chondrite chondrules was evaluated.

1. Host chondrule $\Delta^{17}O$ values in CM chondrites increase continuously from −7‰ to −2‰ with decreasing Mg# from 99 to 37. The majority of types I and II chondrules in CM show high Mg#s ~99 with $\Delta^{17}O$ from −6‰ to −4‰ and lower Mg#s of 60-70 with $\Delta^{17}O$ of −2.5‰, respectively, while a few type I chondrules with lower Mg# (97-93) show $\Delta^{17}O$ between −3.3‰ and −2.5‰, We suggest that bimodal distribution of chondrule Mg# and $\Delta^{17}O$ from Acfer 094 and Y-81020 (CO3) previously reported by Ushikubo et al. (2012) and Tenner et al. (2013), respectively, are parts of the CM chondrule trend.
2. Relict grains in CM chondrite chondrules are either $^{16}O$-rich or $^{16}O$-poor relative to their host chondrules, with the total range from −18‰ to 0‰. The majority of relict grain $\Delta^{17}O$ values overlap the range of host chondrule $\Delta^{17}O$ values, suggesting they were derived from a precursor in the same CM chondrite chondrule forming region. Relict grains with $\Delta^{17}O$ values <−8‰ and ~0‰ are likely from refractory precursors and OC-like precursors, respectively.
3. By adapting the oxygen isotope mass balance model of Tenner et al. (2015) and Hertwig et al. (2018), we argue that the majority of type I chondrules formed under relatively low dust enrichment factors (50-100× Solar) but with a range of $^{16}O$-poor $H_2O$ ice (0-0.8× CI) in the precursors. Other chondrules formed under oxidizing environments with higher dust enrichments (100-1,000× Solar) and abundant $^{16}O$-poor $H_2O$ ice (0.8-1× CI).
4. CM chondrite chondrule formation could have occurred in a large single region that spanned both sides of the snow line, facilitating a wide range of dust-enrichments and $^{16}O$-poor $H_2O$-ice enhancements. It is possible that the conditions in this region evolved with time, from reducing to more oxidizing, as the local disk became denser and colder. This chondrule forming region would have likely exist inside the proto-Jupiter orbit if Jupiter was large enough to produce a gap in the accretion disk.
5. In addition to chondrules, we also analyzed one AOA in Paris, and the data from this AOA are in good agreement with AOAs and other refractory inclusions from Acfer 094, DOM-08006 (CO3), and Murchison (CM2).

## Supplementary Material

Refer to Web version on PubMed Central for supplementary material.

## Acknowledgements

We gratefully thank Brigitte Zanda for allocating us Paris thin sections for the SIMS work. We thank John Fournelle and Jim Kern for assistance with electron probe micro-analysis and SIMS instrument, respectively. We thank Michael Spicuzza for his reading of earlier version of the paper to improving the quality of the manuscript. We thank Kazu Nagashima and Yves Marrocchi for their constructive reviews and Sasha Krot for editorial handling, which improved clarity of the discussions. This work is supported by the NASA Cosmochemistry program (NNX14AG29G). WiscSIMS is partly supported by NSF (EAR13-55590, EAR 1658823).

## REFERENCES

Abreu NM and Brearley AJ (2010) Early solar system processes recorded in the matrices of two highly pristine CR3 carbonaceous chondrites, MET 00426 and QUE 99177. Geochim. Cosmochim. Acta 74, 1146–1171.

Alexander CMO'D, Grossman JN, Ebel DS, and Ciesla FJ (2008) The formation conditions of chondrules and chondrites. Science 320, 1617–1619. [PubMed: 18566282]

Baertschi P (1976) Absolute $^{18}O$ content of standard mean ocean water. Earth Planet. Sci. Lett 31, 341–344.

Berlin J, Jones RH, and Brearley AJ (2011) Fe-Mn systematics of type IIA chondrules in unequilibrated CO, CR, and ordinary chondrites. Meteor. Planet. Sci 45, 513–533.

Bischoff A, Scott ERD, Metzler K, and Goodrich CA (2006) Nature and origins of meteoritic breccias. In Meteorites and the early solar system II, edited by Lauretta DS and McSween HY Jr. Tucson, Arizona: The University of Arizona Press. pp. 679–712.

Brearley AJ (2003) Nebular versus parent-body processing. In Meteorites, comets, and planets, (ed. Davis AM). Vol. 1. *Treatise on Geochemistry* (eds. Holland HD, and Turekian KK) Elsevier-Pergamon, Oxford. pp. 247–268.

Bradley JP and Brownlee DE (1986) Cometary Particles: Thin Sectioning and Electron Beam Analysis. Science 231, 1542–1544. [PubMed: 17833315]

Briani G, Gounelle M, Bourot-Denise M, and Zolensky M (2012) Xenoliths and microxenoliths in H chondrites: Sampling of the zodiacal cloud in the asteroid Main Belt. Meteor. Planet. Sci 47, 880–902.

Budde G, Burkhardt C, Brennecka GA, Fischer-Gödde M, Kruijer TS, Kleine T (2016) Molybdenum isotopic evidence for the origin of chondrules and a dis- tinct genetic heritage of carbonaceous and non-carbonaceous meteorites. Earth Planet. Sci. Lett 454, 293–303.

Busemann H, Alexander CMO'D, and Nittler LR (2007) Characterization of insoluble organic matter in primitive meteorites by microRaman spectroscopy. Meteor. Planet. Sci 42, 1387–1416.

Chakraborty S (2010) Diffusion coefficients in olivine, wadsleyite, and ringwoodite. In Reviews in Mineralogy and Geochemistry, vol. 72 (eds. Zhang Y and Cherniak DJ). Mineralogical Society of America, Washington, DC. pp. 603–639.

Chaumard N, Defouilloy C, and Kita NT (2018) Oxygen isotope systematics of chondrules in the Murchison CM2 chondrite and implications for the CO-CM relationship. Geochim. Cosmochim. Acta 228, 220–242. [PubMed: 30713349]

Clayton RN and Mayeda TK (1999) Oxygen isotope studies of carbonaceous chondrites. Geochim. Cosmochim. Acta 63, 2089–2104.

Clayton RN, Onuma N, Grossman L, and Mayeda TK (1977) Distribution of pre-solar component in Allende and other carbonaceous chondrites. Earth Planet. Sci. Lett. 34, 209–224.

Connolly HC Jr. and Huss GR (2010) Compositional evolution of the protoplanetary disk: oxygen isotopes of type-II chondrules from CR2 chondrites. Geochim. Cosmochim. Acta 74, 2473–2483.

Cuzzi JN, Hogan RC, and Bottke WF (2010) Toward initial mass functions for asteroids and Kuiper Belt objects. Icarus 208, 518–538.

Desch SJ, Kalyaan A and Alexander CMO'D (2018) The effect of Jupiter's formation on the distribution of refractory elements and inclusions in meteorites. Astrophys. J. Suppl. Ser 238, 11.

Donovan JJ (2015) Probe for EPMA v. 11.1.5. User's Guide and References. Probe Software, Inc., Eugene, OR.

Ebel SD and Grossman L (2000) Condensation in dust-enriched systems. Geochim. Cosmochim. Acta 64, 339–366.

Ebert S, Nagashima K, Krot AN, Bischoff A (2020) Oxygen-isotope heterogeneity in the Northwest Africa 3358 (H3.1) refractory inclusions - Fluid-assisted isotopic exchange on the H-chondrite parent body. Geochim. Cosmochim. Acta 282, 98–112.

Eiler JM, Graham C, Valley JW (1997) SIMS analysis of oxygen isotopes: matrix effects in complex minerals and glasses. Chem. Geol 138, 221–244.

Fagan TJ, Krot AN, Keil K and Yurimoto H (2004) Oxygen isotopic evolution of amoeboid olivine aggregates in the reduced CV3 chondrites Efremovka, Vigarano, and Leoville. Geochim. Cosmochim. Acta 68, 2591–2611.

Frank DR, Zolensky ME, and Le L (2014) Olivine in terminal particles of Stardust aerogel tracks and analogous grains in chondrite matrix. Geochim. Cosmochim. Acta 142, 240–259.

Friend P, Hezel DC and Mucerschi D (2016) The conditions of chondrule formation, Part II: Open system. Geochim. Cosmochim. Acta 173, 198–209.

Fukuda K, Brownlee DE, Joswiak DJ, Tenner TJ, Kimura M, and Kita NT (2021) Correlated isotopic and chemical evidence for condensation origins of olivine in comet 81P/Wild 2 and in AOAs from CV and CO chondrites. Geochim. Cosmochim. Acta 293, 544–574.

Gounelle M, Zolensky ME, Liou J-C, Bland PA, and Alard O (2003) Mineralogy of carbonaceous chondritic microclasts in howardites: Identification of C2 fossil micrometeorites. Geochim. Cosmochim. Acta 67, 507–527.

Grossman L and Steele IM (1976) Amoeboid olivine aggregates in the Allende meteorite. Geochim. Cosmochim. Acta 40, 149–155.

Grossman L, Beckett JR, Fedkin AV, Simon SB, and Ciesla FJ (2008) Redox conditions in the solar nebula: Observational, experimental, and theoretical constraints. In Reviews in Mineralogy and Geochemistry, vol. 68 (ed. MacPherson GJ). Mineralogical Society of America, Washington, D.C. pp. 93–140.

Guan Y, McKeegan KD and MacPherson GJ (2000) Oxygen isotopes in calcium-aluminum-rich inclusions from enstatite chondrites: new evidence for a single CAI source in the solar nebula. Earth Planet. Sci. Lett 181, 271–277.

Hartlep T and Cuzzi JN (2020) Cascade Model for Planetesimal Formation by Turbulent Clustering. Astrophys. J 892, 120.

Heck PR, Ushikubo T, Schmitz B, Kita NT, Spicuzza MJ and Valley JW (2010) A single asteroidal source for extraterrestrial Ordivician chromite grains from Sweden and China: high-precision oxygen three-isotope SIMS analysis. Geochim. Cosmochim. Acta 74, 497–509.

Hertwig A, Defouilloy C, and Kita NT (2018) Formation of chondrules in a moderately high dust enriched disk: Evidence from oxygen isotopes of chondrules from the Kaba CV3 chondrite. Geochim. Cosmochim. Acta 224, 116–131. [PubMed: 30713348]

Hertwig AT, Kimura M, Defouilloy C and Kita NT (2019a) Oxygen isotope systematics of chondrule olivine, pyroxene, and plagioclase in one of the most pristine $CV3_{Red}$ chondrites (Northwest Africa 8613). Metorit. Planet. Sci 54, 2666–2685.

Hertwig AT, Kimura M, Ushikubo T, Defouilloy C and Kita NT (2019b) The $^{26}Al$-$^{26}Mg$ systematics of FeO-rich chondrules from Acfer 094: Two chondrule generations distinct in age and oxygen isotope ratios. Geochim. Cosmochim. Acta 253, 111–126. [PubMed: 32214432]

Hewins RH and Zanda B (2012) Chondrules: Precursors and interactions with the nebular gas. Meteorit. Planet. Sci 47, 1120–1138.

Hewins RH, Bourot-Denise M, Zanda B, Leroux H, Barrat J-A, Humayun M, Gopel C, Greenwood RC, Franchi IA, Pont S, Lorand J-P, Cournède C, Gattacceca J, Rochette P, Kuga M, Marrocchi Y, and Marty B (2014) The Paris meteorite, the least altered CM chondrite so far. Geochim. Cosmochim. Acta 124, 190–222.

Hezel DC, Palme H, Nasdala L, Brenker FE, (2006) Origin of SiO2-rich components in ordinary chondrites. Geochim. Cosmochim. Acta 70, 1548–1564.

Itoh S, Russell SS, Yurimoto H (2007) Oxygen and magnesium isotopic compositions of amoeboid olivine aggregates from the Semarkona LL3.0 chondrite. Meteorit. Planet. Sci 42, 1241–1247.

Jones RH (1990) Petrology and mineralogy of type-II, FeO-rich chondrules in Semarkona (LL3.0) – origin by closed-system fractional crystallization, with evidence for supercooling. Geochim. Cosmochim. Acta 54, 1785–1802.

Jones RH (1994) Petrology of FeO-poor, porphyritic pyroxene chondrules in the Semarkona chondrite. Geochim. Cosmochim. Acta 58, 5325–5340.

Jones RH (2012) Petrographic constraints on the diversity of chondrule reservoirs in the protoplanetary disk. Meteorit. Planet. Sci 47, 1176–1190.

Jones RH and Danielson LR (1997) A chondrule origin for dusty relict olivine in unequilibrated chondrites. Meteorit. Planet. Sci 32, 753–760.

Jones RH, Leshin LA, Guan Y, Sharp ZD Durakiewicz T, and Schilk AJ (2004) Oxygen isotope heterogeneity in chondrules from the Mokoia CV3 carbonaceous chondrite. Geochim. Cosmochim. Acta 68, 3423–3438.

Jones RH, Grossman JN, and Rubin AE (2005) Chemical, mineralogical and isotopic properties of chondrules: clues to their origin. In Chondrules and the Protoplanetary Disk, ASP Conference Series (eds. Krot AN, Scott ERD and Reipurth B). Sheridan Books, Ann Arbor, Michigan, pp. 251–285.

Kallemeyn GW and Wasson JT (1981) The compositional classification of chondrites: I. The carbonaceous chondrite groups. Geochim. Cosmochim. Acta 45, 1217–1230.

Kimura M, Grossman JN, and Weisberg MK (2011) Fe-Ni metal and sulfide minerals in CM chondrites: An indicator of thermal history. Meteorit. Planet. Sci. 46, 431–442.

Kimura M, Imae N, Komatsu M, Barrat JA, Greenwood RC, Yamaguchi A, Noguchi T (2020) The most primitive CM chondrites, Asuka 12085, 12169, and 12236, of subtypes 3.0–2.8: Their characteristic features and classification, Polar Science 26, 100565.

Kita NK and Ushikubo T (2012) Evolution of protoplanetary disk inferred from $^{26}$Al chronology of individual chondrules. Meteorit. Planet. Sci 47, 1108–1119.

Kita NT, Ushikubo T, Fu B and Valley JW (2009) High precision SIMS oxygen isotope analysis and the effect of sample topography. Chem. Geol 264, 43–57.

Kita NT, Nagahara H, Tachibana S, Tomomura S, Spicuzza MJ, Fournelle JH and Valley JW (2010) High precision SIMS oxygen three isotope study of chondrules in LL3 chondrites: role of ambient gas during chondrule formation. Geochim. Cosmochim. Acta 74, 6610–6635.

Kita NT, Yin Q-Z, MacPherson GJ, Ushikubo T, Jacobsen B, Nagashima K, Kurahashi E, Krot AN and Jacobsen SB (2013) $^{26}$Al–$^{26}$Mg isotope systematics of the first solids in the early solar system. Meteorit. Planet. Sci 48, 1383–1400.

Kleine T, Budde G, Burkhardt C, Kruijer TS, Worsham EA, Morbidelli A, Nimmo F (2020) he Non-carbonaceous–Carbonaceous Meteorite Dichotomy. Space Sci. Rev 216, 55.

Komatsu M, Fagan TJ, Krot AN, Nagashima K, Petaev MI, Kimura M and Yamaguchi A (2018) First evidence for silica condensation within the solar protoplanetary disk. Proc. Natl. Acad. Sci. USA 115, 7497–7502. [PubMed: 29967181]

Kööp L, Nakashima D, Heck PR, Kita NT, Tenner TJ, Krot AN, Nagashima K, Park C, and Davis AM (2016) New constraints on the relationship between $^{26}$Al and oxygen, calcium, and titanium isotopic variation in the early Solar System from a multielement isotopic study of spinel-hibonite inclusions. Geochim. Cosmochim. Acta 184, 151–172.

Krot AN and Nagashima K (2017) Constraints on mechanisms of chondrule formation from chondrule precursors and chronology of transient heating events in the protoplanetary disk. Geochem. J 51, 45–68.

Krot AN, Libourel G, Goodrich C, Petaev MI (2004) Silica-igneous rims around magnesian chondrules in CR carbonaceous chondrites: evidence for fractional condensation during chondrule formation. Meteorit. Planet. Sci 39, 1931–1955.

Krot AN, Fagan TJ, Nagashima K, Petaev MI and Yurimoto H (2005) Origin of low-Ca pyroxene in amoeboid olivine aggregates: Evidence from oxygen isotopic compositions. Geochim. Cosmochim. Acta 69, 1873–1881.

Krot AN, Yurimoto H, McKeegan KD, Leshin L, Chaussidon M, Libourel G, Yoshitake M, Huss GR, Guan Y, and Zanda B (2006) Oxygen isotopic compositions of chondrules: implications for evolution of oxygen isotopic reservoirs in the inner Solar nebula. Chemie der Erde – Geochem. 66, 249–276.

Krot AN, Park C, Nagashima K (2014) Amoeboid olivine aggregates from CH carbonaceous chondrites. Geochim. Cosmochim. Acta 139, 131–153.

Krot AN, Nagashima K, Libourel G, and Miller KE (2018) Multiple mechanisms of transient heating events in the protoplanetary disk: Evidence from precursors of chondrules and igneous Ca, Al-rich inclusions. In Chondrules: Records of the Protoplanetary Disk Processes. (eds. Russell SS, Connolly HC Jr., and Krot AN) Cambridge University Press, U.K., pp. 11–57.

Kruijer TS Burkhardt C, Budde G, Kleine T (2017) Age of Jupiter inferred from the distinct genetics and formation times of meteorites. Proc. Natl. Acad. Sci. USA 114, 6712–6716. [PubMed: 28607079]

Kunihiro T, Rubin AE, McKeegan KD and Wasson JT (2004) Oxygen-isotopic compositions of relict and host grains in chondrules in the Yamato 81020 CO3.0 chondrite. Geochim. Cosmochim. Acta 68, 3599–3606.

Kunihiro T, Rubin AE and Wasson JT (2005) Oxygen-isotopic compositions of low-FeO relicts in high FeO-host chondrules in Acfer 094, a type 3.0 carbonaceous chondrite closely related to CM. Geochim. Cosmochim. Acta 69, 3831–3840.

Leroux H, Libourel G, Lemelle L, Guyot F (2003) Experimental study and TEM characterization of dusty olivines in chondrites: Evidence for formation by in-situ reduction. Meteorit. Planet. Sci 38, 81–94.

Leroux H, Cuvillier P, Zanda B, and Hewins RH (2015) GEMS-like material in the matrix of the Paris meteorite and the early stages of alteration of CM chondrites. Geochim. Cosmochim. Acta 170, 247–265.

Libourel G and Chaussidon M (2011) Oxygen isotopic constraints on the origin of Mg-rich olivines from chondritic meteorites. Earth Planet. Sci. Lett 301, 9–21.

Libourel G and Portail M (2018) Chondrules as direct thermo- chemical sensors of solar protoplanetary disk gas. Sci. Adv 4, eaar3321. [PubMed: 30009256]

Libourel G, Krot A and Tissandier L (2006) Role of gas-melt interaction during chondrule formation. Earth Planet. Sci. Lett 251, 232–240.

Lin DNC and Papaloizou J (1986) On the tidal interaction between protoplanets and the protoplanetary disk. III—Orbital migration of protoplanets. Astrophys. J 309, 846–857.

Marrocchi Y and Chaussidon M (2015) A systematic for oxygen isotopic variation in meteoritic chondrules. Earth Planet. Sci. Lett 430, 308–315.

Marrocchi Y, Gounelle M, Blanchard I, Caste F, and Kearsley AT (2014), The Paris CM chondrite: Secondary minerals and asteroidal processing. Meteorit Planet Sci 49, 1232–1249.

Marrocchi Y, Villeneuve J, Batanova V, Piani L, Jacquet E (2018) Oxygen isotopic diversity of chondrule precursors and the nebular origin of chondrules. Earth Planet. Sci. Lett 496, 132–141.

Marrocchi Y, Euverte R, Villeneuve J, Batanova V, Welsch B, Ferrière L, Jacquet E (2019) Formation of CV chondrules by recycling of amoeboid olivine aggregate-like precursors. Geochim. Cosmochim. Acta 247, 121–141.

McSween HY (1979) Alteration in CM carbonaceous chondrites inferred from modal and chemical variations in matrix. Geochim. Cosmochim. Acta 43, 1761–1770.

Morbidelli A, Bitsch B, Crida A, Gounelle M, Guillot T, Jacobson S, Johansen A, Lambrechts M, Lega E (2016) Fossilized condensation lines in the Solar System protoplanetary disk. Icarus 267, 368–376.

Nanne JAM, Nimmo F, Cuzzi JN, Kleine T, (2019) Origin of the non- carbonaceous-carbonaceous meteorite dichotomy. Earth Planet. Sci. Lett 511, 44–54.

Nagahara H (1981) Evidence for secondary origin of chondrules. Nature 292, 135–136.

Nagahara H, Kita NT, Ozawa K and Morishita Y (2008) Condensation of major elements during chondrule formation and its implication to the origin of chondrules. Geochim. Cosmochim. Acta 72, 1442–1465.

Nagashima K, Krot AN and Huss GR (2015) Oxygen-isotope compositions of chondrule phenocrysts and matrix grains in Kakangari K-grouplet chondrite: Implication to a chondrule-matrix genetic relationship. Geochim. Cosmochim. Acta 151, 49–67.

Nakamura T (2005) Post-hydration thermal metamorphism of carbonaceous chondrites. J. Mineral. Petrol. Sci 100, 260–274.

Pignatelli I, Marrocchi Y, Vacher LG, Delon R, and Gounelle M (2016) Multiple precursors of secondary mineralogical assemblages in CM chondrites. Meteorit. Planet. Sci 51, 785–805.

Rambaldi ER (1981) Relict grains in chondrules. Nature 292, 558–561. [PubMed: 7254352]

Rubin AE (2013) An amoeboid olivine inclusion (AOI) in CK3 NWA 1559, comparison to AOIs in CV3 Allende, and the origin of AOIs in CK and CV chondrites. Meteorit. Planet. Sci 48, 432–441.

Rubin AE (2015) An American in Paris: Extent of aqueous alteration of a CM chondrite and the petrography of its refractory and amoeboid olivine inclusions. Meteorit. Planet. Sci 50, 1595–1612.

Rubin AE, Trigo-Rodríguez JM, Huber H, and Wasson JT (2007) Progressive aqueous alteration of CM carbonaceous chondrites. Geochim. Cosmochim. Acta 71, 2361–382.

Rudraswami NG, Ushikubo T, Nakashima D and Kita NT (2011) Oxygen isotope systematics of chondrules in the Allende CV3 chondrite: high precision ion microprobe studies. Geochim. Cosmochim. Acta 75, 7596–7611.

Ruzicka A, Hiyagon H, Hutson M, and Floss C (2007) Relict olivine, chondrule recycling, and the evolution of nebular oxygen reservoirs. Earth Planet. Sci. Lett 257, 274–289.

Ruzicka A, Floss C, and Hutson M (2008) Relict olivine grains, chondrules recycling, and implications for the chemical, thermal, and mechanical processing of nebular materials. Geochim. Cosmochim. Acta 72, 5530–5557.

Sakamoto N, Seto Y, Itoh S, Kuramoto K, Fujino K, Nagashima K, Krot AN and Yurimoto H (2007) Remnants of the early solar system water enriched in heavy oxygen isotopes. Science 317, 231–233. [PubMed: 17569827]

Schneider JM, Burkhardt C, Marrocchi Y, Brennecka G, Kleine T (2020) Early evolution of the solar accretion disk inferred from Cr-Ti-O isotopes in individual chondrules. Earth Planet. Sci. Lett 551, 116585.

Schrader DL and Davidson J (2017) CM and CO chondrites: A common parent body or asteroidal neighbors? Insights from chondrule silicates. Geochim. Cosmochim. Acta 214, 157–171.

Schrader DL, Connolly HC Jr., Lauretta DS, Nagashima K, Huss GR, Davidson J and Domanik KJ (2013) The formation and alteration of the Renazzo-like carbonaceous chondrites II: linking O-isotope composition and oxidation state of chondrule olivine. Geochim. Cosmochim. Acta 101, 302–327.

Schrader DL, Nagashima K, Krot AN, Ogliore RC, and Hellebrand E (2014) Variations in the O-isotope composition of gas during the formation of chondrules from the CR chondrites. Geochim. Cosmochim. Acta 132, 50–74.

Schrader DL, Nagashima K, Krot AN, Ogliore RC, Yin Q-Z, Amelin Y, Stirling CH, Kaltenbach A (2017) Distribution of $^{26}$Al in the CR chondrite chondrule-forming region of the protoplanetary disk. Geochim. Cosmochim. Acta 201, 275–302.

Schrader DL, Nagashima K, Fu RR, Davidson J, and Ogliore RC (2020) Outward migration of chondrule fragments in the early Solar System: O-isotopic evidence for rocky material crossing the Jupiter Gap? Geochim. Cosmochim. Acta 282, 133–155.

Sears DWG and Dodd RT (1988) Overview and classification of meteorites. In Meteorites and the early solar system. (eds. Kerridge JF and Matthews MS) University of Arizona Press, Tucson, Arizona, pp 3–31.

Stephant A, Remusat L, and Robert F (2017) Water in type I chondrules of Paris CM chondrite. Geochim. Cosmochim. Acta 199, 75–90.

Sugiura N and Fujya W (2014) Correlated accretion ages and $\varepsilon^{54}$Cr of meteorite parent bodies and the evolution of the solar nebula. Meteorit. Planet. Sci 49, 772–787.

Tachibana S, Nagahara H, Mostefaoui S, and Kita NT (2003) Correlation between relative ages inferred from $^{26}$Al and bulk compositions of ferromagnesian chondrules in least equilibrated ordinary chondrites. Meteorit. Planet. Sci 38, 939–962.

Tanaka H, Murase K, and Tanigawa T (2020) Final masses of giant planets. III. Effect of photoevaporation and a new planetary migration model. Astrophys. J 891, 143.

Tenner TJ, Ushikubo T, Kurahashi E, Kita NT and Nagahara H (2013) Oxygen isotope systematics of chondrule phenocrysts from the CO3.0 chondrite Yamato 81020: evidence for two distinct oxygen isotope reservoirs. Geochim. Cosmochim. Acta 102, 226–245.

Tenner TJ, Nakashima D, Ushikubo T, Kita NT and Weisberg MK (2015) Oxygen isotope ratios of Fe-poor chondrules in CR3 chondrites: Influence of dust enrichment and $H_2O$ during chondrule formation. Geochim. Cosmochim. Acta 148, 228–250.

Tenner TJ, Kimura M, and Kita NT (2017) Oxygen isotope characteristics of chondrules from the Yamato-82094 ungrouped carbonaceous chondrite: Further evidence for common O-isotope environments sampled among carbonaceous chondrites. Meteorit. Planet. Sci 52, 268–294.

Tenner TJ, Ushikubo T, Nakashima D, Schrader DL, Weisberg MK, Kimura M and Kita NT (2018) Oxygen isotope characteristics of chondrules from recent studies by secondary ion mass spectrometry. In Chondrules: Records of the Protoplanetary Disk Processes. (eds. Russell SS, Connolly HC Jr., Krot AN) Cambridge University Press, U.K., pp. 196–246.

Tonui E, Zolensky ME, Hiroi T, Nakamura T, Lipshutz ME, Wang M-S, and Okudaira K (2014) Petrographic, chemical and spectroscopic evidence for thermal metamorphism in carbonaceous chondrites I: CI and CM chondrites. Geochim. Cosmochim. Acta 126, 284–306.

Ushikubo T, Kimura M, Kita NT and Valley JW (2012) Primordial oxygen isotope reservoirs of the solar nebula recorded in chondrules in Acfer 094 carbonaceous chondrite. Geochim. Cosmochim. Acta 90, 242–264.

Ushikubo T, Nakashima D, Kimura M, Tenner TJ and Kita NT (2013) Contemporaneous formation of chondrules in distinct oxygen isotope reservoirs. Geochim. Cosmochim. Acta 109, 280–295.

Ushikubo T, Tenner TJ, Hiyagon H, and Kita NT (2017) A long duration of the $^{16}O$-rich reservoir in the solar nebula, as recorded in fine-grained refractory inclusions from the least metamorphosed carbonaceous chondrites. Geochim. Cosmochim. Acta 201, 103–122.

Vacher LG, Marrocchi Y, Verdier-Paoletti MJ, Villeneuve J, and Gounelle M (2016) Inward radial mixing of interstellar water ices in the solar protoplanetary disk. Astrophys. J. Lett 827, L1.

Vacher LG, Marrocchi Y, Verdier-Paoletti MJ, Villeneuve J, and Gounelle M (2017) Petrographic and C & O isotopic characteristics of the earliest stages of aqueous alteration of CM chondrites. Geochim. Cosmochim. Acta 213, 271–290.

Van Kooten E, Cavalcante L, Wielandt D, and Bizzarro M (2020) The role of Bells in the continuous accretion between the CM and CR chondrite reservoirs. Meteorit. Planet. Sci 55, 575–590. [PubMed: 32362738]

Verdier-Paoletti MJ, Marrocchi Y, Avice G, Roskosz M, Gurenko A, and Gounelle M (2017) Oxygen isotope constraints on the alteration temperatures of CM chondrites. Earth Planet. Sci. Lett 458, 273–281.

Villeneuve J, Libourel G, Soulié C (2015) Relationships between type I and type II chondrules: implications on chondrule formation processes. Geochim. Cosmochim. Acta 160, 277–305

Villeneuve J, Marrocchi Y, Jacquet E (2020) Silicon isotopic compositions of chondrule silicates in carbonaceous chondrites and the formation of primordial solids in the accretion disk. Earth Planet. Sci. Lett 542, 116318.

Wasson JT and Rubin AE (2003) Ubiquitous low-FeO relict grains in type II chondrules and limited overgrowths on phenocrysts following the final melting event. Geochim. Cosmochim. Acta 67, 2239–2250.

Wasson JT, Rubin AE and Yurimoto H (2004) Evidence in CO3.0 chondrules for a drift in the O isotopic composition of the solar nebula. Meteorit. Planet. Sci 39, 1591–1598.

Warren PH (2011) Stable-isotopic anomalies and the accretionary assemblage of the Earth and Mars: A subordinate role for carbonaceous chondrites. Earth Planet. Sci. Lett 311, 93–100.

Weisberg MK, McCoy TJ, and Krot AN (2006) Systematics and evaluation of meteorite classification. In Meteorites and the Early Solar System II (eds. Lauretta DS and McSween HY Jr.) University of Arizona Press, Tucson, Arizona, pp. 19–52.

Weisberg MK, Ebel DS, Connolly HC, Kita NT and Ushikubo T (2011) Petrology and oxygen isotope compositions of chondrules in E3 chondrites. Geochim. Cosmochim. Acta 75, 6556–6569.

Williams CD, Sanborn ME, Defouilloy D, Yin Q-Z, Kita NT, Ebel DS, Yamakawa A and Yamashita K (2020) Chondrules reveal large-scale outward transport of inner Solar System materials in the protoplanetary disk. Proc. Natl. Acad. Sci. USA 117, 23426–23435 [PubMed: 32900966]

Wood JA and Hashimoto A (1993) Mineral equilibrium in fractionated nebular systems. Geochim. Cosmochim. Acta 57, 2377–2388.

Young ED and Russell SS (1998) Oxygen reservoirs in the early solar nebula inferred from an Allende CAI. Science 282, 2377–2388.

Zanda B, Bourot-Denise M, Perron C and Hewins RH (1994) Origin and metamorphic redistribution of silicon, chromium, and phosphorous in the metal of chondrites. Science 265, 1846–1849. [PubMed: 17797224]

Zolensky ME, Barrett R, and Browning L (1993) Mineralogy and composition of matrix and chondrule rims in carbonaceous chondrites. Geochim. Cosmochim. Acta 57, 3123–3148.

Zolensky ME, Weisberg MK, Buchanan PC, Mittlefehldt DW (1996) Mineralogy of carbonaceous chondrite clasts in HED achondrites and the Moon. Meteoritics and Planetary Science 31, 518–537.

Zolensky ME, Mittlefehldt DW, Lipshutz ME, Wang M-S, Clayton RN, Mayeda TK, Grady MM, Pillinger CT, and Barber D (1997) CM chondrites exhibit the complete petrologic range from type 2 to 1. Geochim. Cosmochim. Acta 61, 5099–5115.

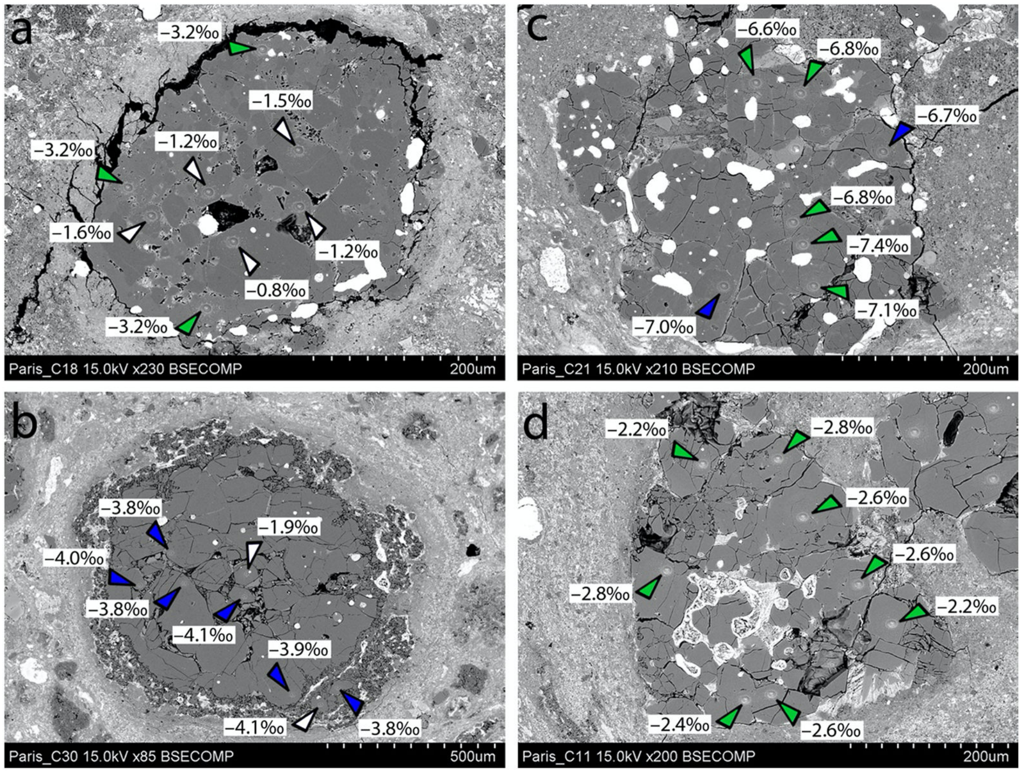


**Fig 1.**

BSE images of type I porphyritic chondrules analyzed in Paris that are homogeneous in terms of oxygen isotope compositions (C18: POP, C30: PO, C21 and C11: PP). SIMS oxygen three-isotope analysis points are shown by the vertex of the triangles, color-coded for mineral phases (olivine: blue, relict olivine: white, low-Ca pyroxene: green). $\Delta^{17}O$ values of individual analyses are indicated.

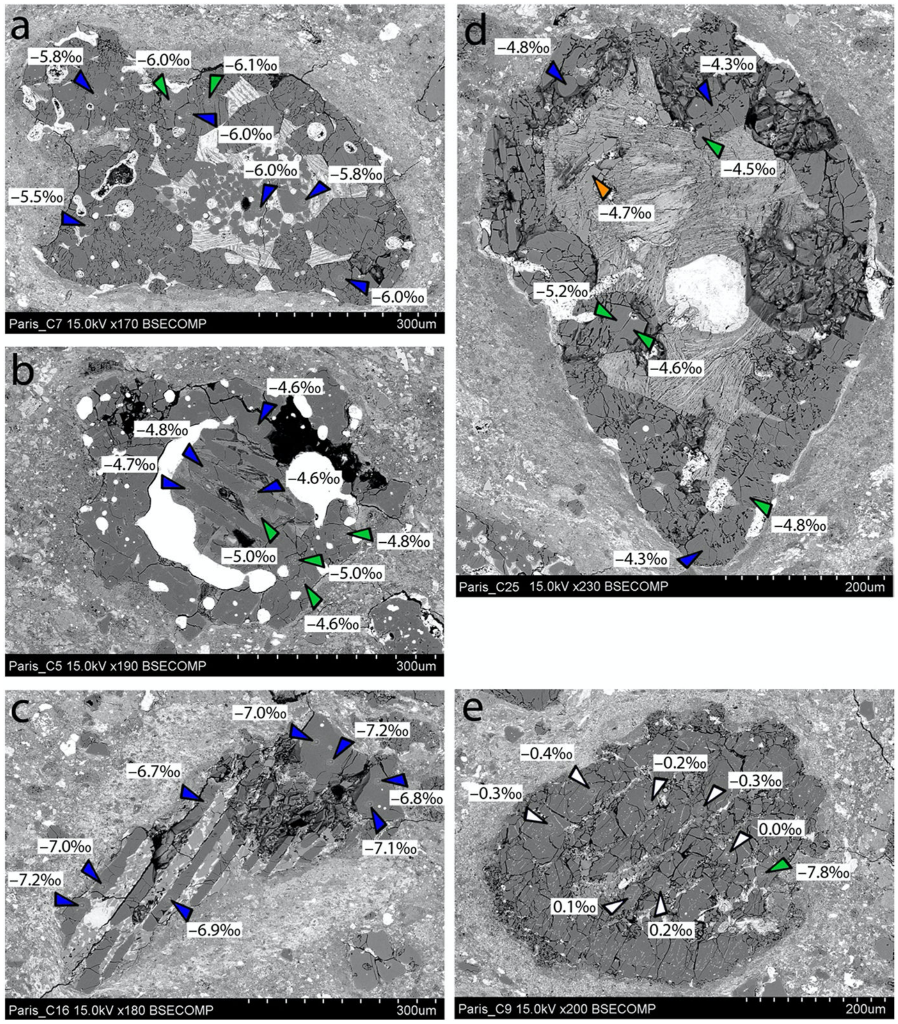


**Fig 2.**

BSE images of type I chondrules analyzed in Paris displaying various textures (C7: POP, C5: POP + BO core, C16: BO fragment, C25: PP, and C9: GO). SIMS oxygen three-isotope analysis points are shown by the vertex of the triangles, color-coded for mineral phases (olivine: blue, relict olivine: white, low-Ca pyroxene: green, high-Ca pyroxene: orange). $\Delta^{17}O$ values of individual analyses are indicated.


NASA Author Manuscript
NASA Author Manuscript

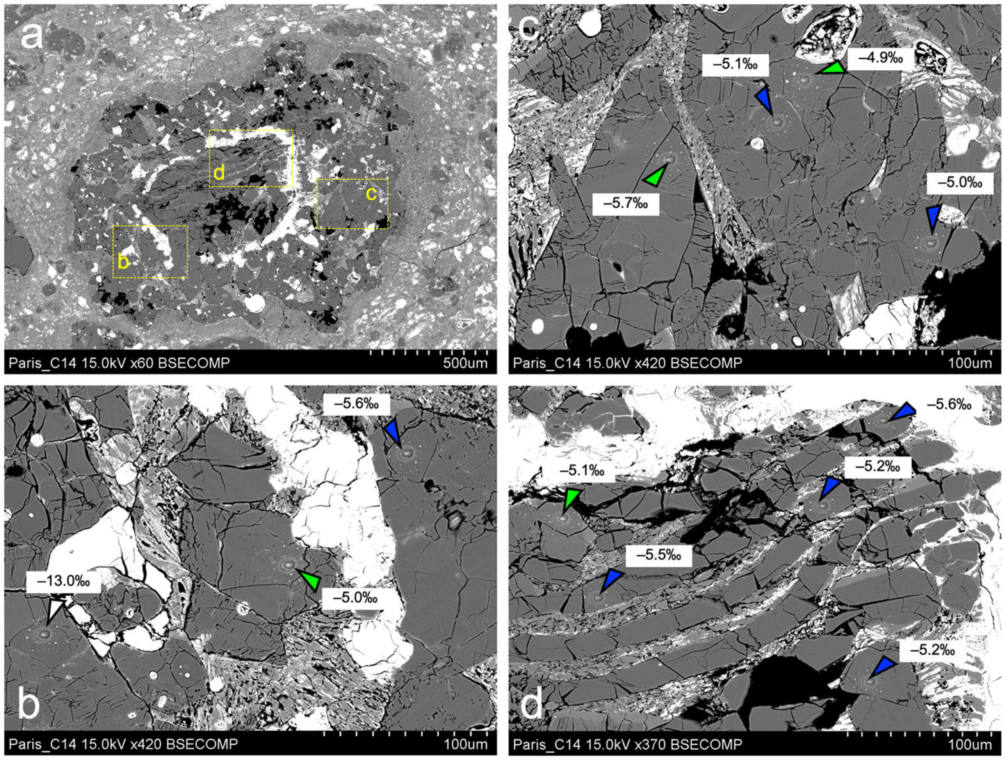


**Fig 3.**

BSE images of the type I chondrule C14 analyzed in Paris. SIMS oxygen three-isotope analysis points are shown by the vertex of the triangles, color-coded for mineral phases (olivine: blue, relict olivine: white, low-Ca pyroxene: green). $\Delta^{17}O$ values of individual analyses are indicated.

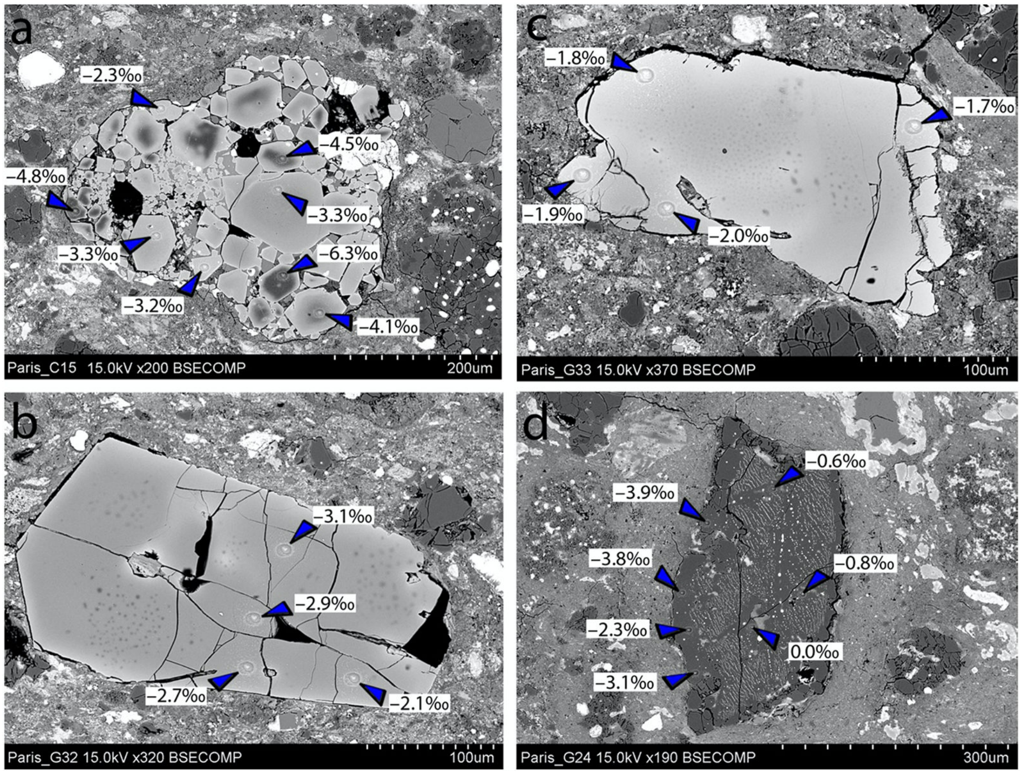


**Fig. 4.**

BSE images of a type II chondrule (C15: PO), two isolated Fe-rich olivine grains (G32 and G33), and an isolated Fe-poor olivine grain (G24) analyzed in Paris. SIMS oxygen three-isotope analysis points are shown by the vertex of the triangles, color-coded for olivine (blue). $\Delta^{17}O$ values of individual analyses are indicated.

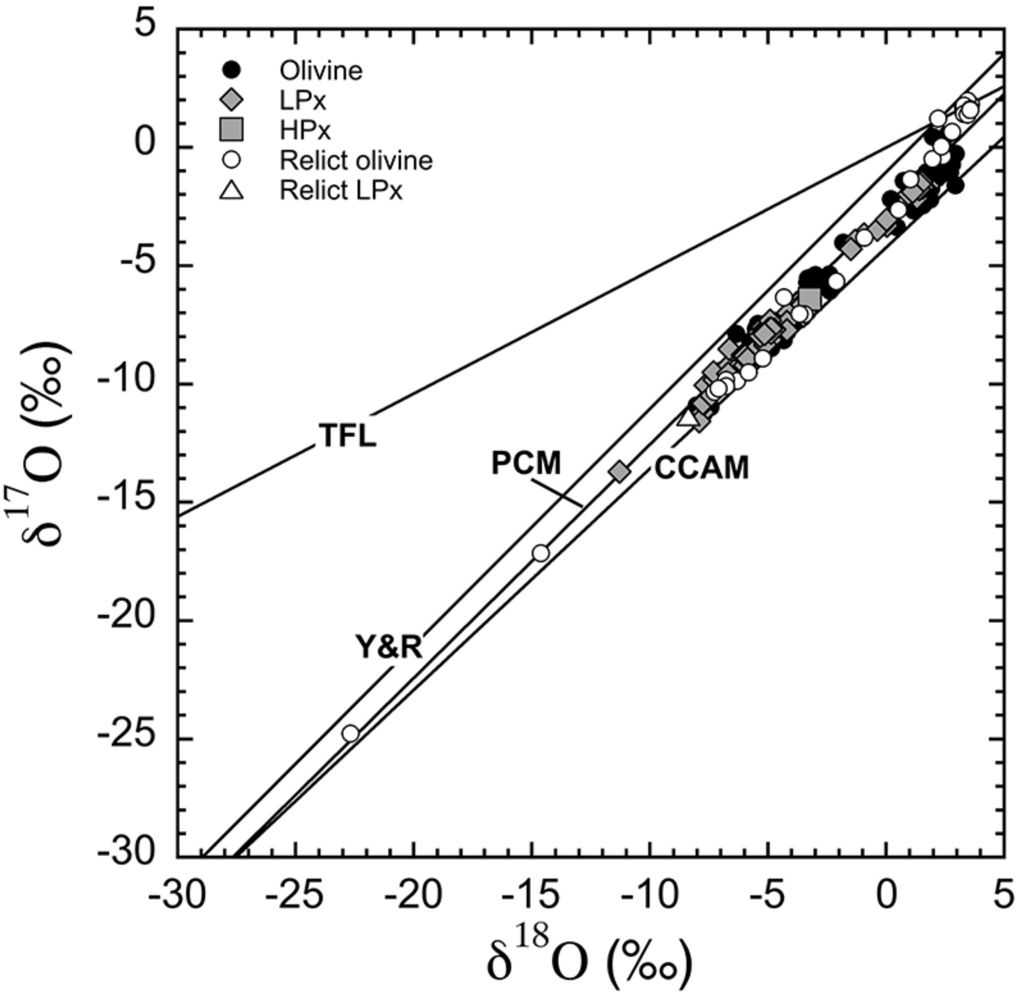


**Fig. 5.**

Oxygen 3-isotope diagram of individual spot analyses of olivine, Low-Ca pyroxene (Lpx), high-Ca pyroxene (Hpx), and relict grains in chondrules in Paris. Error bars, corresponding to the spot-to-spot reproducibility (2SD), are smaller than the symbol sizes. The CCAM (carbonaceous chondrite anhydrous mineral; Clayton et al., 1977), Y&R (Young and Russell, 1998), and PCM (primitive chondrule minerals; Ushikubo et al., 2012) lines are shown for reference. The terrestrial fractionation line (TFL) is also shown.

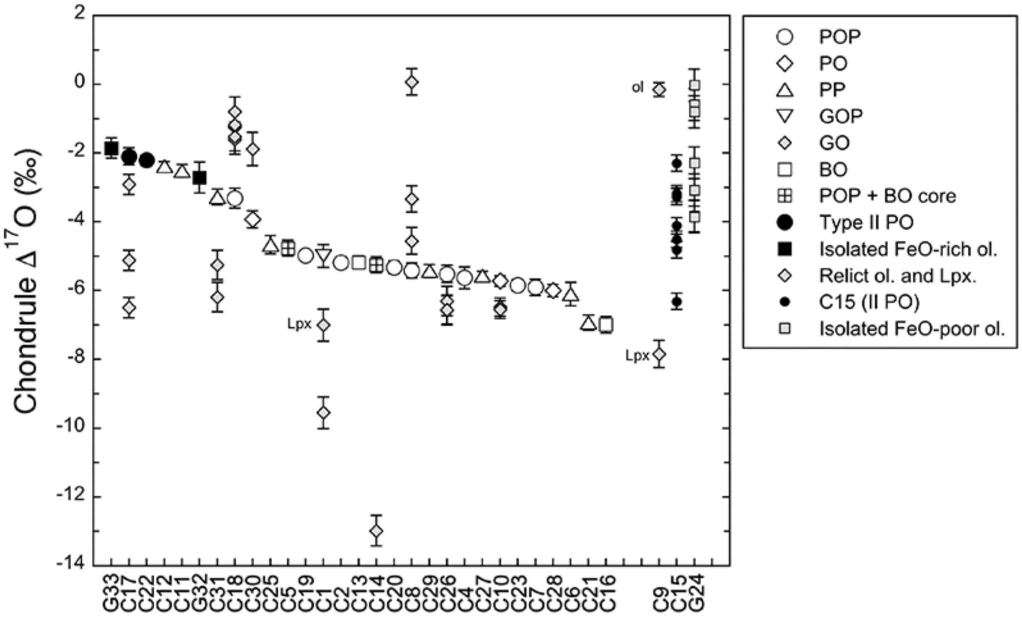


**Fig. 6.**

$\Delta^{17}O$ values of individual host chondrules and isolated olivine grains in Paris. Relict olivine (ol.) and low-Ca pyroxene (Lpx) grains are shown together. Data are sorted according to the host $\Delta^{17}O$ values. Chondrule C9 (GO) contains homogeneously $^{16}O$-poor olivine, which is likely relict. A single analysis of pyroxene would represent melt oxygen isotope ratios that show lower $\Delta^{17}O$ compared to other host chondrule values. For the heterogeneous chondrule C15 (II PO) and isolated Fe-poor olivine grain G24, individual analyses are shown. Error bars represents the propagated uncertainties for host chondrules and olivine in C9 and external reproducibility of individual analyses for relict grains, pyroxene in C9, and all data in C15 and G24.

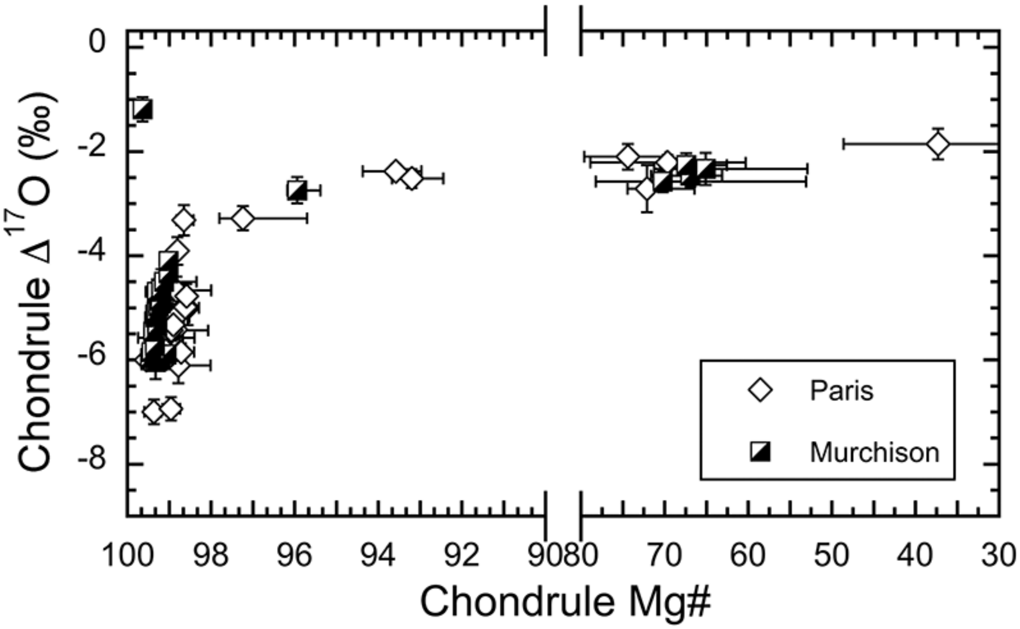


**Fig. 7.**

$\Delta^{17}O$ values of individual host chondrules in Paris vs. Mg#s (open diamonds). Data from the Murchison CM2 chondrite (black and white squares; Chaumard et al., 2018) are shown for comparison. Chondrule Mg# uncertainties correspond to the range of measured values, while uncertainties in $\Delta^{17}O$ are the propagated 2SE.

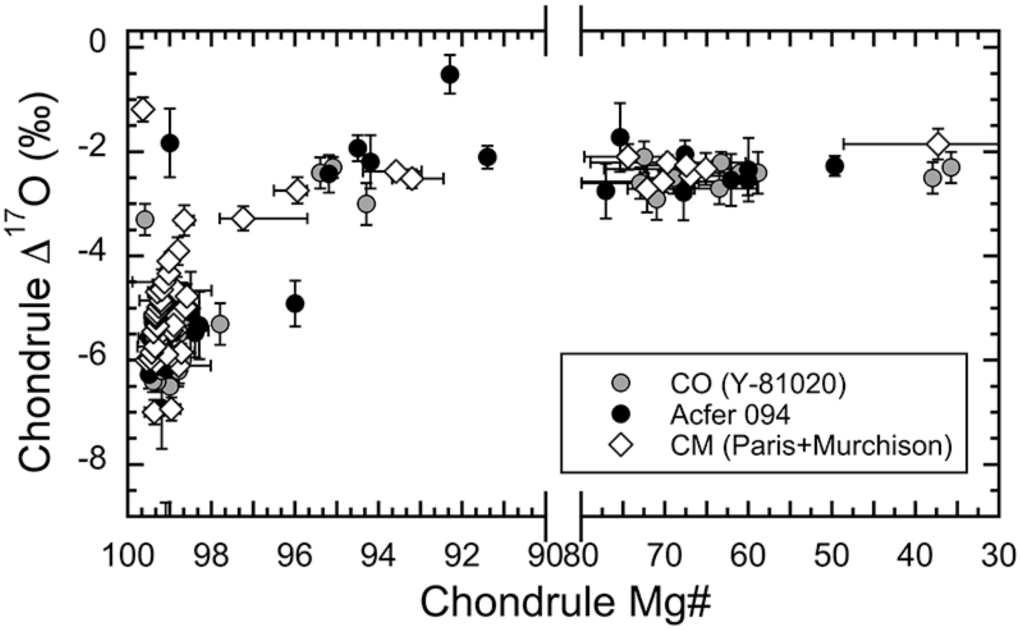


**Fig. 8.**

$\Delta^{17}O$ values vs. Mg#s of individual host chondrules in CM (open diamonds; Chaumard et al., 2018; this work), CO (grey circles; Tenner et al., 2013), and Acfer 094 (black circles; Ushikubo et al., 2012) chondrites. Chondrule Mg# uncertainties correspond to the range of measured values, while uncertainties in $\Delta^{17}O$ are the propagated 2SE.

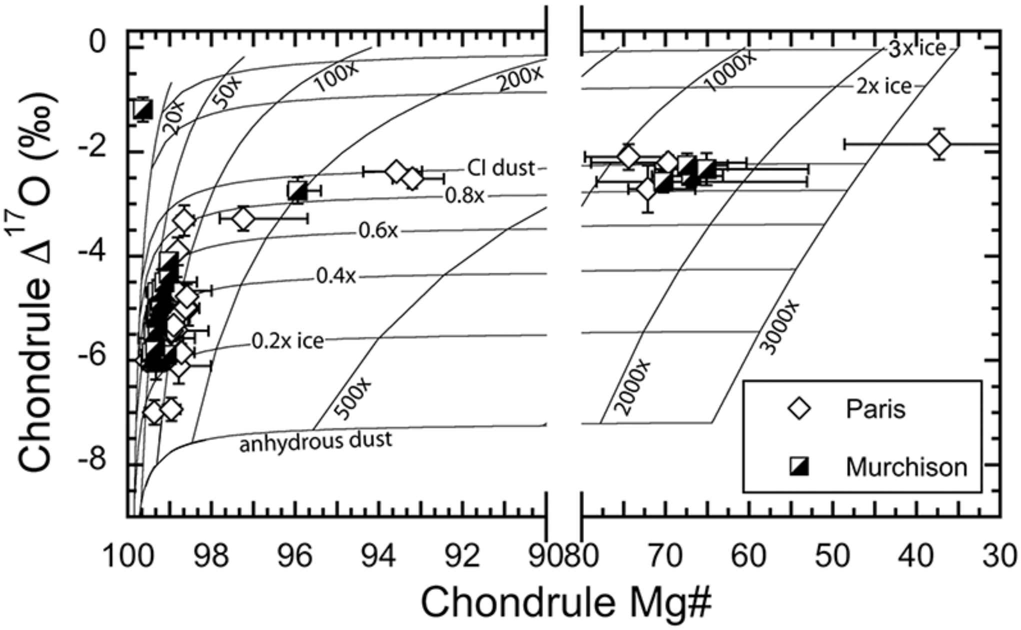


**Fig. 9.**

$\Delta^{17}O$ values of individual host chondrules in the CM chondrites Paris (this work) and Murchison (Chaumard et al., 2018) and Mg#s superimposed by oxygen isotope mixing curves of constant dust enrichment and ice enhancement from Tenner at el. (2015) and Hertwig et al. (2018). In this model, the anhydrous silicate dust, Solar gas, water ice, and organics in the dust are considered to have $\Delta^{17}O$ values of −8.0‰, −28.4‰, +2.0‰, and +11.3‰, respectively (Hertwig et al., 2018). Chondrule Mg# uncertainties correspond to the range of measured values, while uncertainties in $\Delta^{17}O$ are the propagated 2SE.

NASA Author Manuscript
NASA Author Manuscript

**Table 1.**

Mg#'s and O-isotope ratios of host chondrules and relict grains.

| Chondrule | Type, texture | Mg# [a] | +/− [b] | n (ol, lpx, hpx) [c] | $\delta^{18}O$ | unc. | $\delta^{17}O$ | unc. | $\Delta^{17}O$ | unc. | $\Delta^{17}O$ 2SD | Beam (μm) |
|---|---|---|---|---|---|---|---|---|---|---|---|---|
| **Homogeneous** | | | | | | | | | | | | |
| C21 | I, PP | 99.0 | 0.2/0.3 | 2,5,0 | −7.7 | 0.3 | −10.9 | 0.3 | −6.93 | 0.22 | 0.6 | 15 |
| C6 | I, PP | 98.8 | 0.3/0.8 | 2,4,0 | −6.5 | 0.4 | −9.5 | 0.4 | −6.10 | 0.34 | 0.3 | 15 |
| C28 | I, PO | 99.6 | 0.1/0.2 | 8,0,0 | −6.3 | 0.3 | −9.3 | 0.3 | −5.99 | 0.18 | 0.4 | 15 |
| C23 | I, POP | 98.7 | 0.3/0.3 | 3,4,0 | −5.7 | 0.6 | −8.8 | 0.3 | −5.84 | 0.17 | 0.4 | 15 |
| C10 | I, PO | 99.2 | 0.1/0.2 | 5,1,0 | −6.4 | 0.5 | −9.1 | 0.3 | −5.72 | 0.16 | 0.3 | 15 |
| | relict ol | 99.3 | n.a. | 1,0,0 | −5.8 | 0.2 | −9.5 | 0.3 | −6.5 | 0.3 | n.a. | 15 |
| | relict ol | 99.0 | n.a. | 1,0,0 | −7.3 | 0.2 | −10.3 | 0.3 | −6.6 | 0.3 | n.a. | 15 |
| C27 | I, PP | 99.3 | 0.5/0.9 | 6,2,0 | −4.5 | 0.4 | −7.9 | 0.3 | −5.57 | 0.13 | 0.2 | 15 |
| C4 | I, POP | 99.0 | 0.2/0.3 | 6,2,0 | −5.9 | 0.4 | −8.7 | 0.4 | −5.63 | 0.31 | 0.2 | 15 |
| C26 | I, POP | 99.0 | 0.1/0.1 | 2,3,0 | −4.7 | 0.4 | −7.9 | 0.3 | −5.51 | 0.25 | 0.4 | 15 |
| | relict ol | 99.3 | n.a. | 1,0,0 | −6.8 | 0.2 | −9.8 | 0.5 | −6.3 | 0.4 | n.a. | 15 |
| | relict ol | 99.3 | n.a. | 1,0,0 | −6.8 | 0.2 | −10.1 | 0.5 | −6.6 | 0.4 | n.a. | 15 |
| | relict ol | 99.2 | n.a. | 1,0,0 | −6.3 | 0.2 | −9.9 | 0.5 | −6.6 | 0.4 | n.a. | 15 |
| C29 | I, PP | 99.0 | 0.3/0.9 | 2,4,0 | −4.8 | 0.4 | −7.9 | 0.3 | −5.43 | 0.19 | 0.4 | 15 |
| C20 | I, POP | 98.9 | 0.4/0.2 | 4,5,0 | −5.0 | 0.3 | −7.9 | 0.2 | −5.32 | 0.18 | 0.4 | 15 |
| C13 | I, BO | 99.1 | 0.2/0.1 | 4,0,0 | −4.2 | 0.4 | −7.4 | 0.3 | −5.18 | 0.19 | 0.3 | 15 |
| C2 | I, POP | 98.9 | 0.3/0.4 | 4,4,0 | −4.8 | 0.4 | −7.7 | 0.2 | −5.19 | 0.17 | 0.4 | 15 |
| C19 | I, POP | 98.6 | 0.2/0.2 | 5,3,0 | −4.8 | 0.3 | −7.5 | 0.2 | −4.98 | 0.14 | 0.3 | 15 |
| C30 | I, PO | 98.8 | 0.1/0.1 | 6,0,0 | −3.2 | 0.3 | −5.6 | 0.3 | −3.90 | 0.26 | 0.2 | 15 |
| | relict ol | 98.7 | n.a. | 1,0,0 | 1.0 | 0.3 | −1.3 | 0.4 | −1.9 | 0.5 | n.a. | 15 |
| | relict ol | 98.4 | n.a. | 1,0,0 | −4.3 | 0.3 | −6.3 | 0.4 | −4.1 | 0.5 | n.a. | 15 |
| C18 | I, POP | 98.7 | 0.1/0.3 | 0,3,0 | −1.2 | 0.5 | −4.0 | 0.4 | −3.31 | 0.29 | 0.4 | 15 |
| | relict ol | 99.3 | n.a. | 1,0,0 | 2.8 | 0.2 | 0.7 | 0.5 | −0.8 | 0.4 | n.a. | 15 |
| | relict ol | 99.1 | n.a. | 1,0,0 | 2.4 | 0.2 | 0.0 | 0.5 | −1.2 | 0.4 | n.a. | 15 |
| | relict ol | 99.1 | n.a. | 1,0,0 | 2.3 | 0.2 | 0.0 | 0.5 | −1.2 | 0.4 | n.a. | 15 |
| | relict ol | 99.1 | n.a. | 1,0,0 | 2.0 | 0.2 | −0.5 | 0.5 | −1.5 | 0.4 | n.a. | 15 |
| | relict ol | 99.1 | n.a. | 1,0,0 | 2.4 | 0.2 | −0.4 | 0.5 | −1.6 | 0.4 | n.a. | 15 |

NASA Author Manuscript
NASA Author Manuscript

| Chondrule | Type, texture | Mg# [a] | +/− [b] | n (ol, lpx, hpx) [c] | $\delta^{18}O$ | unc. | $\delta^{17}O$ | unc. | $\Delta^{17}O$ | unc. | $\Delta^{17}O$ 2SD | Beam (μm) |
|---|---|---|---|---|---|---|---|---|---|---|---|---|
| C11 | I, PP | 93.2 | 0.2/0.7 | 0,8,0 | 1.5 | 0.3 | −1.7 | 0.3 | −2.51 | 0.18 | 0.5 | 15 |
| C12 | I, PP | 93.6 | 0.8/0.6 | 0,7,0 | 1.3 | 0.4 | −1.7 | 0.2 | −2.37 | 0.13 | 0.3 | 15 |
| C16 | I, BO, frag. | 99.4 | 0.2/0.2 | 8,0,0 | −7.9 | 0.4 | −11.1 | 0.3 | −6.99 | 0.24 | 0.4 | 10 |
| C7 | I, POP | 99.0 | 0.1/0.2 | 6,2,0 | −6.7 | 0.5 | −9.4 | 0.4 | −5.90 | 0.24 | 0.4 | 10 |
| C8 | I, POP | 98.9 | 0.0/0.1 | 3,2,0 | −5.3 | 0.4 | −8.2 | 0.3 | −5.42 | 0.22 | 0.4 | 10 |
| | relict ol | 98.8 | n.a. | 1,0,0 | 2.2 | 0.4 | 1.2 | 0.4 | 0.1 | 0.4 | n.a. | 10 |
| | relict ol | 98.7 | n.a. | 1,0,0 | −2.1 | 0.4 | −5.7 | 0.4 | −4.6 | 0.4 | n.a. | 10 |
| | relict ol | 98.7 | n.a. | 1,0,0 | −0.9 | 0.4 | −3.8 | 0.4 | −3.3 | 0.4 | n.a. | 10 |
| C14 | I, POP+BO core | 99.0 | 0.2/0.3 | 7,4,0 | −5.3 | 0.5 | −8.0 | 0.3 | −5.26 | 0.23 | 0.6 | 10 |
| | relict ol | 99.1 | n.a. | 1,0,0 | −22.7 | 0.3 | −24.8 | 0.4 | −13.0 | 0.4 | n.a. | 10 |
| C1 | I, GOP | 98.6 | 0.3/0.3 | 2,3,0 | −3.7 | 0.5 | −6.9 | 0.4 | −4.99 | 0.33 | 0.6 | 10 |
| | relict ol | 99.0 | n.a. | 1,0,0 | −14.6 | 0.6 | −17.2 | 0.6 | −9.5 | 0.5 | n.a. | 10 |
| | relict lpx | 98.8 | n.a. | 0,1,0 | −8.4 | 0.6 | −11.4 | 0.6 | −7.0 | 0.5 | n.a. | 10 |
| C25 | I, PP | 98.8 | 0.4/0.8 | 3,4,1 | −3.2 | 0.4 | −6.3 | 0.4 | −4.66 | 0.26 | 0.6 | 10 |
| C5 | I, POP+BO core | 98.6 | 0.2/0.3 | 4,4,0 | −4.8 | 0.8 | −7.3 | 0.4 | −4.77 | 0.23 | 0.4 | 10 |
| C31 | I, PP | 97.3 | 0.5/1.6 | 1,5,0 | 0.0 | 0.4 | −3.3 | 0.4 | −3.28 | 0.23 | 0.4 | 10 |
| | relict ol | 97.8 | n.a. | 1,0,0 | −3.5 | 0.5 | −7.1 | 0.6 | −5.3 | 0.4 | n.a. | 10 |
| | relict ol | 97.6 | n.a. | 1,0,0 | −5.2 | 0.5 | −8.9 | 0.6 | −6.2 | 0.4 | n.a. | 10 |
| C22 | II, PO | 69.7 | 9.3/9.4 | 7,0,0 | 2.3 | 0.4 | −1.0 | 0.3 | −2.21 | 0.15 | 0.3 | 15 |
| C17 | II, PO | 74.4 | 5.2/4.5 | 5,0,0 | 2.8 | 0.3 | −0.6 | 0.3 | −2.09 | 0.25 | 0.5 | 15 |
| | relict ol | 99 | n.a. | 1,0,0 | −7.1 | 0.1 | −10.2 | 0.3 | −6.5 | 0.3 | n.a. | 15 |
| | relict ol | 76.6 | n.a. | 1,0,0 | −3.7 | 0.1 | −7.0 | 0.3 | −5.1 | 0.3 | n.a. | 15 |
| | relict ol | 71.4 | n.a. | 1,0,0 | 0.5 | 0.1 | −2.6 | 0.3 | −2.9 | 0.3 | n.a. | 15 |
| **Heterogeneous** | | | | | | | | | | | | |
| C9 | I, GO | 99.4 | 0.1/0.1 | 7,0,0 | 3.5 | 0.4 | 1.7 | 0.3 | −0.15 | 0.20 | 0.4 | 10 |
| | | 99.3 | n.a. | 0,1,0 | −11.3 | 0.4 | −13.7 | 0.4 | −7.8 | 0.4 | n.a. | 10 |
| C15 | II, PO | 98.5 | n.a. | 1,0,0 | −6.6 | 0.1 | −9.8 | 0.2 | −6.3 | 0.2 | n.a. | 15 |
| | | 98.3 | n.a. | 1,0,0 | −3.4 | 0.1 | −6.6 | 0.2 | −4.8 | 0.2 | n.a. | 15 |
| | | 97.7 | n.a. | 1,0,0 | −2.6 | 0.1 | −5.9 | 0.2 | −4.5 | 0.2 | n.a. | 15 |
| | | 91.3 | n.a. | 1,0,0 | −2.4 | 0.1 | −5.4 | 0.2 | −4.1 | 0.2 | n.a. | 15 |

| Chondrule | Type, texture | Mg# [a] | +/− [b] | n (ol, lpx, hpx) [c] | $\delta^{18}O$ | unc. | $\delta^{17}O$ | unc. | $\Delta^{17}O$ | unc. | $\Delta^{17}O$ 2SD | Beam (µm) |
|---|---|---|---|---|---|---|---|---|---|---|---|---|
| | | 77.3 | n.a. | 1,0,0 | 1.2 | 0.1 | −2.7 | 0.2 | −3.3 | 0.2 | n.a. | 15 |
| | | 66.9 | n.a. | 1,0,0 | 1.6 | 0.1 | −2.4 | 0.2 | −3.3 | 0.2 | n.a. | 15 |
| | | 63.4 | n.a. | 1,0,0 | 2.5 | 0.1 | −1.0 | 0.2 | −2.3 | 0.2 | n.a. | 15 |
| | | 58.9 | n.a. | 1,0,0 | 1.9 | 0.1 | −2.2 | 0.2 | −3.2 | 0.2 | n.a. | 15 |

[a] Mg# = Mg/(Fe+Mg) molar % of olivine and/or pyroxene in each chondrule.

[b] Uncertainties represent the range in measured Mg#'s of olivine and/or pyroxenes.

[c] Numbers of mineral phases analyzed (olivine, low-Ca pyroxene, and high-Ca pyroxene).




NASA Author Manuscript
NASA Author Manuscript

**Table 2.**

Mg#'s and O-isotope ratios of isolated olivine grains and aggregate olivine inclusion.

| Object | Type, texture | Mg# | +/− | n (ol) | $\delta^{18}O$ | unc. | $\delta^{17}O$ | unc. | $\Delta^{17}O$ | unc. | $\Delta^{17}O$ 2SD | Beam (μm) |
|---|---|---|---|---|---|---|---|---|---|---|---|---|
| *G32* | Isolated FeO-rich olivine | 72.2 | 2.3/5.7 | 4 | 2.2 | 0.7 | −1.6 | 0.5 | −2.7 | 0.5 | 0.8 | 15 |
| *G33* | Isolated FeO-rich olivine | 37.3 | 11.4/7.7 | 4 | 1.8 | 0.9 | −0.9 | 0.5 | −1.9 | 0.3 | 0.3 | 15 |
| G24 | Isolated FeO-poor olivine | 99.4 | n.c. | 1 | 3.3 | 0.3 | 1.7 | 0.5 | 0.0 | 0.5 | n.a. | 10 |
| | | 99.4 | n.c. | 1 | 2.0 | 0.3 | 0.4 | 0.5 | −0.6 | 0.5 | n.a. | 10 |
| | | 99.4 | n.c. | 1 | −1.8 | 0.3 | −4.0 | 0.5 | −3.1 | 0.5 | n.a. | 10 |
| | | 99.4 | n.c. | 1 | −3.2 | 0.3 | −5.5 | 0.5 | −3.8 | 0.5 | n.a. | 10 |
| | | 99.3 | n.c. | 1 | 2.6 | 0.3 | 0.6 | 0.5 | −0.8 | 0.5 | n.a. | 10 |
| | | 99.3 | n.c. | 1 | 0.2 | 0.3 | −2.2 | 0.5 | −2.3 | 0.5 | n.a. | 10 |
| | | 99.3 | n.c. | 1 | −3.1 | 0.3 | −5.4 | 0.5 | −3.9 | 0.5 | n.a. | 10 |
| I3 | AOI | 99.5 | 0.1/0.0 | 2 | −45.5 | 0.5 | −47.3 | 0.4 | −23.7 | 0.2 | 0.4 | 10 |